Statistical Study of Traveling Ionospheric Disturbances over South Africa

A thesis submitted in fulfillment of the requirements for the degree of

MASTERS OF SCIENCE

OF

RHODES UNIVERSITY

BY

Daniel Fiso Mahlangu

December 2017

Abstract

This thesis provides a statistical analysis of traveling ionospheric disturbances (TIDs) in South Africa. The velocities of the TIDs were determined from total electron content (TEC) maps using particle image velocimetry (PIV). The periods were determined using Morlet function in wavelet analysis. The TIDs were grouped into four categories: daytime, twilight, nighttime TIDs, and those TIDs that occurred during magnetic storms. It was found that daytime medium scale TIDs (MSTIDs) propagated equatorward in all seasons (summer, autumn, winter, and spring), with velocities of about 114 to 213 m/s. Their maximum occurrence was in winter between 15:00 and 16:00 LT. The daytime large scale (TIDs) LSTIDs propagated equatorward with velocities of approximately 455 to 767 m/s. Their highest occurrence was in summer, between 12:00-13:00 LT. Most of the these TIDs (about 78%) were observed during the passing of the morning solar terminator. This implied that the morning terminator was more effective in instigating TIDs. Only a few nighttime TIDs were observed and therefore their behavior could not be statistically inferred. The TIDs that occurred during magnetically disturbed conditions propagated equatorward. This indicated that their source mechanism was atmospheric gravity waves generated at the onset of geomagnetic storms.

Acknowledgments

First and foremost I thank God, it is through His grace that the project was possible. I would like to extend my sincere gratitude to my supervisors (Dr Zama Thobeka Katamzi-Joseph and Dr John Bosco Habarulema) for their support and guidance. I thank the South African National Space Agency (SANSA), this project would have not be completed without their resources, and financial support. I am also grateful to the Rhodes University for providing me with an opportunity to undertake my studies.

My stay at SANSA has been wonderful, thanks to my friendly colleagues, and housemates at the residence. Lastly, I thank my family for their encouragement and inspiration.

Contents

List of Tables

List of Figures

Chapter 1

Introduction

1.1 General background

The ionosphere is an ionized region of the Earth's atmosphere which is found at altitudes of about 50 to 1000 km (Dieminger *et al.*, 1996; Goodman, 2005); it is used as a medium of propagation for high frequency (HF) radio waves in HF communication. This is done by transmitting HF waves from the ground into the ionosphere, where electrons will refract and reflect the waves to a receiver on the ground (McNamara, 1991). This refractive and reflective property allows HF waves to propagate great distances, allowing long distance communication. However ionospheric refraction causes undesirable delays on transionospheric radio signals like those transmitted by Global Positioning System (GPS) satellites and celestial bodies. If the ionospheric electron density were to remain constant over time, it would be straightforward to apply refraction corrections to these signals. As a result, accurate GPS positioning and timing would be achieved. However, the electron density is not uniform, both in space and time; it contains horizontal gradients and temporal fluctuations (Rawer, 1993). Although large horizontal gradients are more or less predictable, the small-scale irregularities are not. Hence it is difficult to predict their effects on radio signals (Rawer, 1993; Kintner *et al.*, 2008).

These unpredictable irregularities may occur as stationary or moving structures (Rawer, 1993). The latter are referred to as traveling ionospheric disturbances (TIDs) (Rawer, 1993; Hargreaves, 1979). TIDs are said to be ionospheric manifestations of atmospheric gravity waves (AGWs) (Hines, 1960). AGWs are up and down movement of displaced air parcel in the atmosphere, in response to buoyancy force (Nappo, 2002). In order to understand the behavior of TIDs, it is important to perform a comprehensive study that will characterize their occurrence in a particular region. This can be achieved using different ionospheric probing instruments such as Earth orbiting satellites which transmit radio frequencies (e.g. Bhonsle *et al.*, 1965; Bhonsle, 1966; Habarulema *et al.*, 2015), ionosondes (e.g. Heisler and Whitehead, 1960; Afraimovich *et al.*, 2008), incoherent scatter radar and super dual auroral radar network (SuperDARN) (e.g. Thome, 1960; Karpachev, 2010).

In this project, radio signals from Earth orbiting satellites were used to create maps of total electron content (TEC) over South Africa for the year 2010. TEC is defined as the total electron density from a GPS receiver to an Earth-orbiting transmitting satellite along an imaginary cylinder with a cross-sectional area of 1 m^2 (Hofmann-Wellenhof *et al.*, 1992). The year 2010 was chosen so as to compare this study with previous work on TIDs characteristics in South Africa, using a different method. TIDs were identified as TEC peaks or troughs from subsequent TEC maps. TEC measurements of 30 seconds cadence were chosen because of availability of a dense network of GPS receivers (about 54 receivers) located over South Africa, hence there were enough data to create maps of electron density.

1.2 Aims of the Thesis

Comprehensive studies on TIDs in South Africa were performed by Chum *et al.* (2012), Sindelarova *et al.* (2012) and Tyalimpi (2014). However, their studies were limited to only the south-west part of the country (the Western Cape). Therefore, there is still a need to perform more investigations in the southern Africa. As a result, in this project, the aims are to:

- Determine the propagation characteristics of TIDs in South Africa using TEC data.
- Perform statistical analysis on TIDs that occurred in 2010. This includes seasonal dependence and preferred propagation direction.

1.3 Structure of the Thesis

The structure of this thesis is as follows:

- Chapter 2 discusses a background theory of the ionosphere. That is its creation, morphology, and its behavior.
- In Chapter 3, the background theory on AGWs and their signatures as TIDs are discussed. Furthermore, a detailed literature review on TIDs in the mid-latitudes is given.
- Chapter 4 provides an introduction to GPS, and demonstrates how TEC data were obtained from GPS. Also, the methods used to determine periods and velocities of TIDs from TEC maps are discussed.

- In Chapter 5, results obtained by applying methods described in Chapter 4 are presented and discussed.
- Chapter 6 is the conclusion of the thesis.

Chapter 2

The Ionosphere

2.1 Formation

At ionospheric heights, the Earth's atmosphere is composed mainly of oxygen, nitrogen, nitric oxide, helium, and hydrogen (Hargreaves, 1979). The ionosphere is formed when these constituents are photoionized by highly energetic solar radiation (Ratcliffe, 1960; McNamara, 1991). As the solar radiation penetrates the atmosphere from high to low altitudes, its intensity decreases due to absorption by neutral atoms and molecules. As a result, less plasma is produced in the lower atmosphere. On the other hand, the density of atmospheric atoms and molecules increases as altitude decreases. These opposing trends of the radiation intensity and atmospheric density result in a maximum electron production at some high altitude (McNamara, 1991).

At the same time that photoionization occurs, some electrons are lost through processes known as attachment and recombination. In the lower ionosphere, electrons are lost through attachment as they directly combine with neutral molecules or atoms to form negatively charged particles (McNamara, 1991).

Recombination occurs when electrons combine with oppositely charged molecules or atoms to form neutral gas (Dieminger *et al.*, 1996). When an electron (denoted by e^-) combines with a positive ion (X^+) to form a neutral atom (X) as illustrated by

$$X^+ + e^- \longrightarrow X + \text{photon},$$

the process is known as radiative recombination, as a photon is produced (Prölss, 2004).

Another type of recombination is dissociative recombination and it is the most dominant in the ionosphere. It occurs in two stages; in the first stage charge exchange occurs when (X^+) species collide with neutral molecular (A_2) species:

$$X^+ + A_2 \longrightarrow AX^+ + A.$$

This is called the β -type reaction, and it occurs at the rate $L = \beta[X^+]$, where β is the attachment coefficient and $[X^+]$ is the concentration of X^+ (Ratcliffe, 1972; Hargreaves, 1979). The second stage of dissociative recombination occurs when the charged molecule produced by the β-type reaction is dissociated by an electron (e^-):

$$AX^+ + e^- \longrightarrow A + X.$$

This type of reaction (α-type) occurs at the rate $L = \alpha N_e^2$, where α is the dissociative coefficient (Ratcliffe, 1972; Hargreaves, 1979; McNamara, 1991; Dieminger *et al.*, 1996). Hargreaves (1979) further stated that β is larger than α in the lower ionosphere, hence AX^+ is produced at a higher rate; which leaves the α-type reaction to regulate electron loss rate. Conversely α is greater in the upper ionosphere, which means that electrons rapidly dissociate charged molecules; leaving the β-type reaction to regulate neutralization.

2.2 Morphology

The ionosphere is divided into two parts: the bottomside and topside. The bottomside is further vertically subdivided into three strata, namely the D, E and F regions (see Figure 2.1A). During the day, the F region splits into two subregions: F1 and F2 (in this thesis, F1 and F2 will be identified as layers.) Each region/layer has a peak of electron density (N_{max}) at a particular height (McNamara, 1991). Ionosondes, sounding radars which operate at different frequencies in the HF band, are generally used to determine N_{max} of each region (Dobson, 1968; Goodman, 2005). A wave transmitted by an ionosonde will experience refraction of an index given by

$$n = \sqrt{1 - \left(\frac{f_N}{f}\right)^2}, \tag{2.1}$$

as it propagates in the ionosphere; with

$$f_N = 8.98\sqrt{N_e}. \tag{2.2}$$

The frequencies f_N and f are for free oscillating ionospheric electrons and that of the transmitted wave, respectively (Hargreaves, 1979; Goodman, 2005). According to Ratcliffe (1972), the ionosphere will reflect the wave when f_N equals f, i.e., when n in Equation 2.1 equals zero; in such a scenario, f is referred to as the critical frequency (f_c in Equation 2.3). Critical frequency is defined as the maximum frequency that can be reflected by a particular region or layer. There are three critical frequencies corresponding to the E region, F1 and F2 layers.

$$f_c = 8.98\sqrt{N_{max}}. \tag{2.3}$$

2.2.1 The D Region

This region occurs at altitudes from about 50 to 90 km (Dieminger *et al.*, 1996) (see Figure 2.1A). The electron density in the D region is much less than molecular density. As a result collision frequency between electrons and molecules (such as O_3, NO, NO_2, CO_2 and H_2O) is high. Therefore energy absorbed by electrons from HF waves is lost to the molecules during the collision process, leading to high absorption of HF waves in this region (Rishbeth and Garriott, 1969; Ratcliffe, 1972). As a result, this makes it difficult to study the D region using ionosondes. Alternative methods like long waves have been used instead (Rishbeth and Garriott, 1969).

2.2.2 The E Region

The E region is found at altitudes of about 90 to 160 km, with N_{max} at about 110 km, as depicted in Figure 2.1A. The E region occurs in two forms: the normal E and sporadic E (Es) (Hargreaves, 1992). The normal E region mainly comprises O_2^{2+} and NO^+ ions. These ions are produced when X-rays of wavelength 10 Å to 100 Å ionize O_2 and NO, respectively (Hargreaves, 1992). The E region is a Chapman layer, which means that its critical frequency (f_oE) is dependent on the solar zenith angle (χ) as shown by

$$f_oE = 900(\frac{q_o}{\alpha}\cos\chi)^{0.25}, \tag{2.4}$$

where q_o is the peak electron production rate, α is the dissociative recombination coefficient and χ is the solar zenith angle (Rishbeth and Garriott, 1969).

Es occur at E region heights with a thickness of a few kilometers and span a few hundred kilometers (McNamara, 1991). What sets a sporadic E apart from the normal E region is that it contains a higher electron density, its occurrence is unpredictable, and it does not obey the Chapman theory (Thomas and Smith, 1959; Hargreaves, 1992). In the mid-latitudes, maximum electron density of Es occurs at about 90 to 130 km altitude (McNamara, 1991). In addition to solar radiation, ion production in the Es is driven by wind shear at E region heights (Dieminger *et al.*, 1996). The shearing is due to variations of wind speed with altitude; in the presence of the geomagnetic field, the winds can compress the E region plasma to form Es (Hargreaves, 1992).

2.2.3 The F Region

The F region occurs from altitudes of about 160 to 350 km (see Figure 2.1A) (Kamide and Chain, 2007); its ionization processes are driven by extreme ultraviolet (EUV) rays of 200 Å to about 1100 Å wavelength (Hargreaves, 1979). The F1 layer extends from about 160 to 210 km with the critical frequency ($foF1$) occurring at about 180 km (Dobson, 1968; Hargreaves, 1992; Goodman, 2005). NO^+ and O_2^+ are the major ion constituents of this layer (Zolesi and Cander, 2014). The F1 layer follows the Chapman theory of electron production, as it can be see from (Goodman, 2005)

$$f_oF1 \propto (\cos\chi)^{0.2}. \tag{2.5}$$

The F2 layer extends from about 210 to 350 km with critical frequency $foF2$ at about 350 km (Kamide and Chain, 2007). The most ionized part of the ionosphere, with O^+ and He^+ being the most dominant ions (Dieminger *et al.*, 1996; Goodman, 2005). The existence of the F2 layer during daytime and nighttime enables HF communication throughout the day (Zolesi and Cander, 2014).

2.2.4 The Topside

The topside is found at altitudes above 350 to about 1000 km, it is mainly composed of O^+ ions (Kamide and Chain, 2007). The electron density decreases exponentially with height (Kamide and Chain, 2007). Hence any radio wave that is transmitted from the ground cannot be reflected by this region. As a result, the topside cannot be observed using ground-based ionosondes. For many years, since 1962, information about topside came from sounders onboard satellites (Hargreaves, 1979; Dieminger *et al.*, 1996). Recently low Earth orbit satellites, such as Constellation Observing System for Meteorology, Ionosphere, and Climate (COSMIC) (Anthes *et al.*, 2008), and SWARM have been used to study TEC of the topside (Pedatella *et al.*, 2011; Buchert *et al.*, 2015).

2.3 Ionospheric Variations

2.3.1 Diurnal Variations

Diurnal variations of critical frequencies in the E region, F1 and F2 layers measured by ionosonde are shown in Figure 2.1B. Since the D region is known for absorbing HF waves, its diurnal variations cannot be studied by ionosondes like E and F regions. However, this does not imply the absence of the D region. According to McNamara (1991), the D region is present during the day because of the availability of solar X-rays which ionize some of the constituents. At nighttime, the D region vanishes because recombination and electron attachment dominate (McNamara, 1991; Dieminger *et al.*, 1996).

It can be seen from Figure 2.1B that during the day f_oE, f_oF1 and f_oF2 show a similar behavior; they increase from the morning hours until they reach maximum values around noon. Figure 2.1B suggests that the E region disappears at night due to absence of solar radiation. However, McNamara (1991) states that the E region does not completely disappear at night, instead f_oE decreases significantly such that it does not reflect HF waves.

The F1 layer completely disappears after sunset, as it is indistinguishable from the F2 layer. Moreover, the F2 layer persists throughout the night as shown in Figure 2.1B. This is due to thermospheric neutral winds that push the F region plasma upward to altitudes where recombination is low (Ondoh and Marubashi, 2000).

2.3.2 Seasonal Variations

Figure 2.2A is a plot of f_oF2 over a period of one year. In winter f_oF2 decreases to its lowest, and then increases in summer. However, at times a seasonal anomaly occurs. This is when f_oF2 is higher in winter as opposed to summer (Dieminger *et al.*, 1996). Ondoh and Marubashi (2000) stated that the seasonal anomaly is caused by an imbalance in $[O_2]$ and $[N_2]$. Hargreaves (1979) further stated that atomic oxygen is mainly responsible for electron production in the F2 layer, whereas O_2 and N_2 are mainly responsible for recombination. In summer, atomic oxygen density decreases due to global atmospheric circulation. As a result the ratios $[O]/[O_2]$ and $[O]/[N_2]$ decrease, which implies less electron production in summer (Hargreaves, 1979; Ondoh

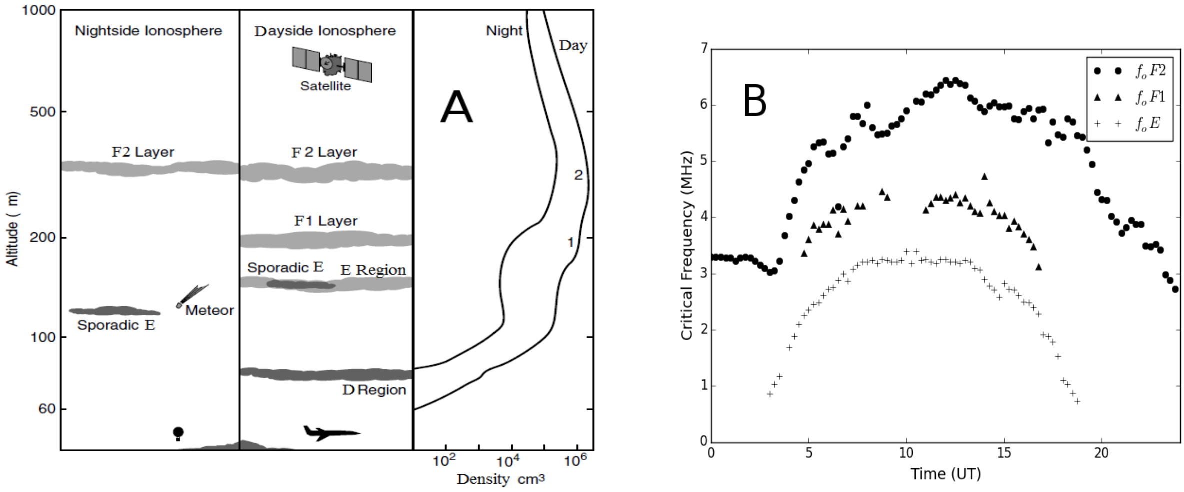

Figure 2.1: Nighttime and daytime structure of the ionosphere in the mid-latitude (A) (Moldwin, 2008), and its diurnal variation observed in Hermanus on 2010-01-01 (B).

and Marubashi, 2000; Prölss, 2004). Hence there is higher electron density in the F2 layer during winter compared to summer. Furthermore, there are noticeable broad peaks of f_oF2 at equinoxes (see Figure 2.2). These peaks are what is known as the semiannual anomaly. Zou *et al.* (2000) explained this as being due to thermospheric circulation. Following this finding, Rishbeth *et al.* (2000) stated that the seasonal behavior of [O]/[N_2] symmetric about winter, hence the semiannual anomaly is observed.

The F1 layer and the E region show an expected seasonal behavior as can be seen in Figure 2.2B and C, respectively. In summer the solar zenith angle is smaller, therefore electron production is higher, than in winter (Ondoh and Marubashi, 2000).

The seasonal behavior of the D region can be understood by studying HF wave absorption throughout the year (Hargreaves, 1979). The D region absorption varies with solar zenith angle, as a result higher absorption occurs in summer as opposed to winter (Ratcliffe, 1960; Hargreaves, 1979). However this is not always the case, there are times when high absorption is observed in winter than in summer (Ratcliffe, 1960). According to Hargreaves (1979) the D region absorption is influenced by seasonal changes of the chemistry of the atmosphere, in particular the variations in [NO]. In winter [NO] is higher compared to summer; consequently, more electrons are produced in winter when NO is photoionized. This leads to an increase in N_e, which results in high collision frequency between electrons and molecules. Hence there is high HF absorption in the D region during winter compared to summer (Dobson, 1968; Hargreaves, 1979). This anomalous behavior of the D region is known as the winter absorption (Ratcliffe, 1960).

2.3.3 Solar Cycle Variations

The Sun's influence on ionospheric electron production varies as solar emission activities change with time. Long-term solar effect on the ionosphere can be understood by studying the relationship between critical frequencies and solar indices such as

- the sunspot number (R),
- solar flare occurrence rate (N_f),
- solar radio emission ($F_{10.7}$),
- and hydrogen Lyman-α (Lym-α) (Hargreaves, 1979; Perna and Pezzopane, 2016).

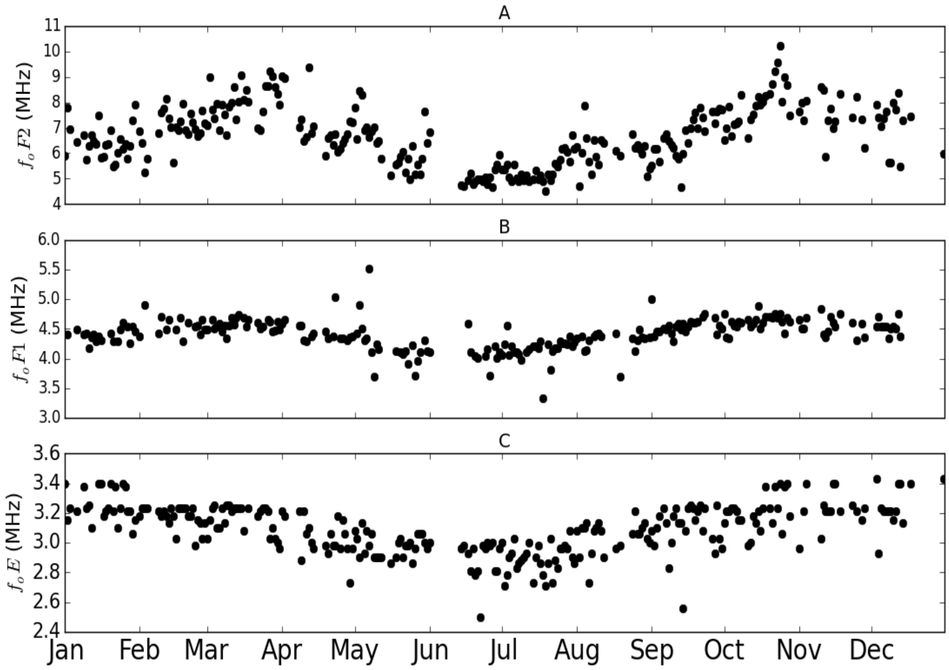

Figure 2.2: Annual variations of f_oF2 (A), f_oF1 (B) and f_oE (C) at 10:00 UT (12:00 LT) for the year 2010. These measurements were acquired by an ionosonde located in Hermanus.

Sunspots are dark areas that occur in groups on the Sun's surface (the photosphere), and can be observed through an optical telescope (Hargreaves, 1979). The sunspot number is defined by

$$\mathrm{R} = k(f + 10g_s), \tag{2.6}$$

where k is a constant related to the sensitivity of the observing instrument, f is the total number of sunspots visible to the observer, and g_s is the number of sunspot groups observed (Hargreaves, 1979). Through an optical telescope, solar flares appear as sudden brighting patches near sunspots (Hargreaves, 1979). Solar flares are associated with an ejection of stream of protons and electrons from the photosphere, and an increase radiation intensity (X-radiation and ultraviolet) (Dobson, 1968). The solar flare occurrence rate is defined as the number of flares per 27 days (solar rotation); it is given by

$$\mathrm{N}_f = \alpha_s(\mathrm{R}_{mean} + 10), \tag{2.7}$$

where R_{mean} is the mean sunspot number and α_s is a constant between 1.5 and 2 (Hargreaves, 1979). $\mathrm{F}_{10.7}$ is the radio flux (measured in 10^{-22} $\mathrm{m}^{-2}\mathrm{Hz}^{-1}$) emitted by the Sun at 10.7 cm wavelength (Ondoh and Marubashi, 2000). The hydrogen Lyman-α is the solar emission at 121.6 nm (Hargreaves, 1979; Perna and Pezzopane, 2016). Long-term monitoring of these indices shows a sinusoidal trend with a period of approximately 11 years (known as the solar cycle), where the crests and troughs are known as solar maxima and minima, respectively (Ratcliffe, 1960; Hargreaves, 1979; Perna and Pezzopane, 2016).

At solar maximum, when R is high, the production of solar flares increases, this can be seen from Equation 2.7. Since solar flares are accompanied by high radiation intensities and charged particles, the ionosphere experiences an increase in electron density during high solar activity. As a result, the D region electron and molecule collision frequency increases, and subsequently absorption is increased. Furthermore, electron density in the E and F regions follows the same trend as the solar cycle (Ratcliffe, 1960; McNamara, 1991). Figure 2.3 shows f_oF2 (obtained from Grahamstown station) against R, $\mathrm{F}_{10.7}$ and Lym-α from 2001 to 2015, at 10:00 UT (12:00 LT). In order to minimize seasonal variations in the data, 356 days running means were computed from the both critical frequencies and solar indices (Perna and Pezzopane, 2016). It can be seen from the figure that ionospheric variations are in-phase with the solar cycle. This shows a strong correlation between solar activity and ionospheric ionization (Perna and Pezzopane, 2016).

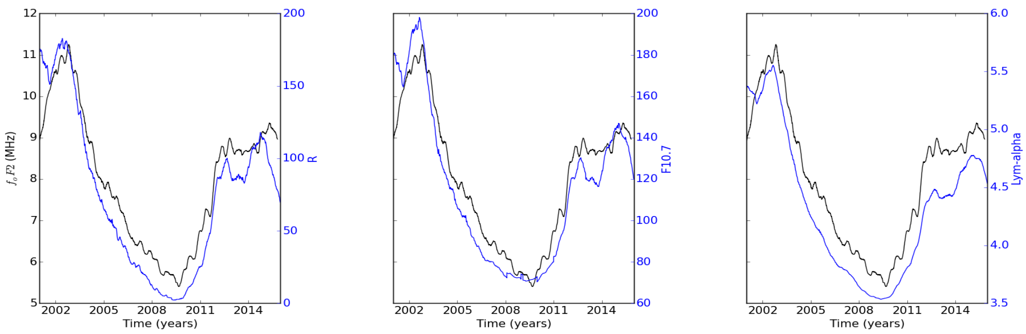

Figure 2.3: Long term variations of f_oF2, R, $F_{10.7}$ and Lym-α.

2.3.4 Effects of Storms on the Ionosphere

A storm is defined as a severe departure from normal ionospheric or geomagnetic behavior which usually lasts from one to few days (Hargreaves, 1992). In this thesis two types of storms are discussed: geomagnetic (or magnetic) and ionospheric storm. According to Hargreaves (1992) and Gonzalez *et al.* (1994) a magnetic storm is defined as severe fluctuations of the geomagnetic field. Such fluctuations can be caused by charged particles from solar winds which bombard the geomagnetic field. A solar wind approaching the Earth contains an interplanetary magnetic field (IMF) which interacts with the geomagnetic field on arrival (Hargreaves, 1979; Gonzalez *et al.*, 1994). A magnetic storm occurs if the southward component of the IMF interacts with the geomagnetic field such that the solar wind particles are injected into the Earth's magnetosphere (Dieminger *et al.*, 1996; Tsurutani *et al.*, 1997; Borovsky and Denton, 2006).

Solar winds which normally cause magnetic storms are those which are delivered to the geomagnetic field by coronal mass ejections (CMEs) or corotating interacting regions (CIRs) (Borovsky and Denton, 2006). A CME is a large cloud of charged particles released by the Sun, mostly during solar maximum (Hargreaves, 1979). A CIR consists of high speed streams of charged solar particles which are released by low temperature regions (coronal holes) on the photosphere (Borovsky and Denton, 2006). Most CIRs are observed during the declining phase of the solar cycle because the Sun is dominated by coronal holes at this phase (Tsurutani *et al.*, 1997). It is important to distinguish between CMEs and CIRs since they cause magnetic storms of different nature. The main features that set the two storm drivers (CMEs and CIRs) apart are: CMEs contain a higher particle density compared to CIRs, and IMFs associated with CMEs are of higher strengths (Borovsky and Denton, 2006).

The severity of a magnetic storm in the mid-latitude is widely measured by the Dst (expressed in nanoTelsa, nT), and the Kp indices. The Dst index measures how much the Earth's horizontal component of the geomagnetic field is reduced at the magnetic equator by ring currents (Desseler and Parcker, 1959). Ring currents are electric currents that encircle the Earth during a magnetic storm (Hargreaves, 1979). Table 2.1 categorizes the severity of a storm into five levels (Loewe and Prölss, 1997). The Kp index measures the global magnetic field variations at the mid-latitudes (Moldwin, 2008). The measure of a storm intensity expressed by a natural number from 0 to 9, where Kp = 0 indicate no magnetic activity and Kp = 9 implies a major activity. However, on average anything greater than Kp = 3 is regarded as a magnetic storm (Hargreaves, 1992; Moldwin, 2008).

Table 2.1: Categories of a geomagnetic of storm according to the Dst index (Loewe and Prölss, 1997).

Dst (nT)	Storm category
$-30 \geq \text{Dst} > -50$	Small
$-50 \geq \text{Dst} > -100$	Moderate
$-100 \geq \text{Dst} > -200$	Intense
$-200 \geq \text{Dst} \geq -350$	Strong
$\text{Dst} < -350$	Great

Other differences between CME and CIR-driven storms are that CME-driven storms have shorter duration and stronger Dst, while CIR-driven storms have longer duration and weaker Dst (Borovsky and Denton, 2006). Moreover, the commencement of most CME-driven storms is seen by a sudden increase in Dst, indicating the arrival of dense solar plasma on the geomagnetic field; this is known as the sudden storm commencement (SSC) (Gonzalez *et al.*, 1994). The SSC marks the beginning of the first of three CME-driven storm phases: initial, main and recovery. In the initial phase the horizontal component of the magnetic field increases for a few hours. This is caused by the dense solar plasma compressing the magnetosphere upon its arrival. The main phase occurs when the horizontal magnetic field decreases until it reaches a minimum value. The recovery phase is when the magnetic field is regaining its normal state (Hargreaves, 1979). Normally CIR-driven storms do not contain the initial phase because of the weaker impact of CIR on the Earth's magnetic field, hence they have a weaker Dst (Borovsky and Denton, 2006). Typical signatures of CME and CIR-driven magnetic storms are depicted on the left and right of Figure 2.4, respectively.

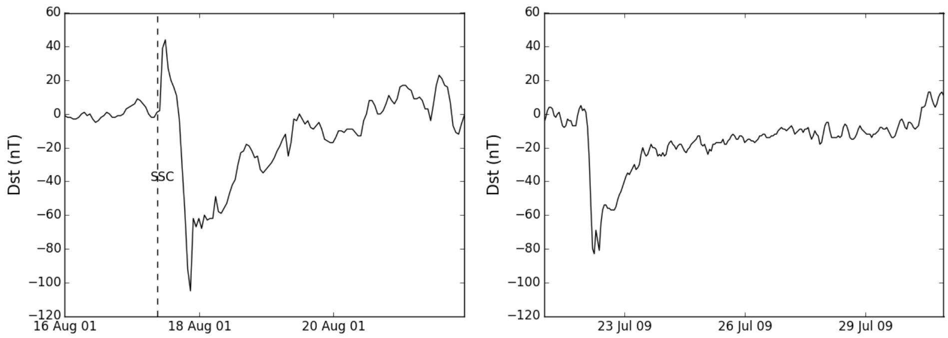

Figure 2.4: An intense CME-driven magnetic storm that occurred on 2001-8-17 (left). The SSC is depicted by a dashed line. A moderate CIR-driven magnetic storm that occurred on 2009-7-22 (right).

An ionospheric storm is defined as a deviation of electron density from a normal behavior in response to magnetic storms (Hargreaves, 1992). In the F2 layer, an ionospheric storm can be seen by a decrease or increase in f_oF2. When f_oF2 is decreased the ionospheric storm is said to be negative, and when it is increased the storm is termed positive (McNamara, 1991). During a positive storm the D region electron density is enhanced; this can be seen by an increase in HF wave absorption (Ratcliffe, 1960), and by a lower reflection altitude for very low frequency waves (Hargreaves, 1992). This effect occurs mainly during the main phase of the magnetic storms, however, during large storms it may persist even during the recovery phase in what is known as the post storm effects (Hargreaves, 1992).

A negative storm usually displays features that resemble the magnetic storm: the initial phase occurs when the electron density increase for a few hours, followed by the main phase which results from f_oF2 being reduced to values below normal conditions, and lastly the recovery phase where f_oF2 returns to normal (Hargreaves, 1992). These electron density changes are accompanied by altitude changes and thickness increase of the F2 layer (Hargreaves, 1992; Foster and Rich, 1998).

Chapter 3

Atmospheric Gravity Waves

This chapter provides the background theory of atmospheric conditions necessary for AGWs to propagate. Furthermore, the dispersion relation for AGWs is derived, and will be used to demonstrate the difference between AGWs and sound (acoustic) waves in the atmosphere. Possible sources and modes of propagation of AGWs will also be discussed. Moreover, the response of the ionosphere due to AGWs excitation will be demonstrated. Lastly, TIDs, which are manifestations of AGWs (Hines, 1960; Hocke and Schlegel, 1996) will be discussed with reference to previous work.

3.1 Atmospheric Hydrostatic Equilibrium

The Earth's atmosphere is assumed to be an isothermal ideal gas, with the equation of state given by

$$p = \rho R T, \tag{3.1}$$

where p is pressure, ρ is density, $R = 287$ J kg^{-1}K^{-1} is the universal gas constant and T is the average temperature (Nappo, 2002). In the absence of any vertical motion, the atmosphere is approximated to be in hydrostatic equilibrium. This means that an upward pressure acting on an air parcel of density ρ, with a unit area ($dxdy = 1$) at height dz is in balance with its weight ($-\rho g dz$) (Nappo, 2002), i.e.,

$$dp = -\rho g dz, \tag{3.2}$$

where dp is the unit pressure. The negative sign means that the weight is directed downwards, and $g = 9.8$ m/s^2 is the Earth's gravity. Equation 3.2 can be written as

$$\frac{dp}{dz} = -\rho g. \tag{3.3}$$

Equation 3.3 is known as the hydrostatic equation (Beer, 1974; Nappo, 2002). Substituting Equation 3.1 into Equation 3.3 leads to

$$\frac{1}{\rho}\frac{d\rho}{dz} = -\frac{g}{RT}. \tag{3.4}$$

Integrating

$$\frac{1}{\rho}d\rho = -\frac{g}{RT}dz \tag{3.5}$$

leads to

$$\rho(z) = \rho_i \exp\left(-z/H\right), \tag{3.6}$$

where ρ_i is the atmospheric density at the Earth's surface, and $H = \frac{RT}{g}$ is known as the scale height. Equation 3.6 suggests that the density of a stable atmosphere decreases with altitude.

3.2 Buoyancy Force

If a stable atmosphere is disturbed such that an air parcel is displaced vertically, the Earth's gravity and atmospheric compressibility will act in order to restore equilibrium (Beer, 1974; Nappo, 2002). Consider an air parcel in a stable atmosphere at height z; its density (ρ_0) is the same as that of the surroundings (ρ). If the parcel is displaced from z to $z + \Delta z$, the hydrostatic equilibrium will be disturbed. According to the law of propagation of sound in a fluid, and assuming that the displacement occurs adiabatically (Beer, 1974), the density change ($\Delta\rho_1$) is given by

$$\Delta\rho_1 = \frac{\Delta p}{C^2}, \tag{3.7}$$

where p is the ambient pressure and C is the speed of sound. Since the surrounding is in hydrostatic equilibrium, Equation 3.3 implies that $\Delta p = -\rho g \Delta z$. The change in density with height for the surrounding atmosphere is $\frac{d\rho_0}{dz}$. Therefore, over the displacement Δz, the density will be changed by $\Delta\rho_2$, which is given by

$$\Delta\rho_2 = \frac{d\rho_0}{dz}\Delta z. \tag{3.8}$$

It is clear from Equations 3.7 and 3.8 that at height $z + \Delta z$ the density of the air parcel and that of the surroundings are not equal. Therefore the restoring buoyancy force is

$$F_b = g(\Delta\rho_2 - \Delta\rho_1), \tag{3.9}$$

as defined by Nappo (2002). Newton's second law of motion for the air parcel is given by

$$\rho_0 \frac{d^2(\Delta z)}{dt^2} = g\Big(\frac{d\rho_0}{dz} + \frac{\rho_0 g}{C^2}\Big)\Delta z. \tag{3.10}$$

Equation 3.10 represents a simple harmonic motion with a solution of the form

$$\Delta z(t) = Ae^{i\omega_B t} + Be^{-i\omega_B t}, \tag{3.11}$$

where A and B are constants, $i = \sqrt{-1}$ and ω_B is the oscillation frequency. The second-order time derivative of Equation 3.11 is

$$\frac{d^2(\Delta z)}{dt^2} = -\omega_B^2 \Delta z. \tag{3.12}$$

Substituting Equation 3.12 into Equation 3.10 leads to

$$\omega_B^2 = -\frac{g}{\rho_0}\Big(\frac{d\rho_0}{dz} + \frac{\rho_0 g}{C^2}\Big), \tag{3.13}$$

ω_B is known as the Brunt-Väisälä frequency (Beer, 1974; Kohl *et al.*, 1996). The speed of sound in an isothermal atmosphere is given by

$$C^2 = \gamma p_0/\rho_0 = \gamma g H, \tag{3.14}$$

where γ is the ratio of specific heats at constant pressure and volume (Kelly, 2009). The Brunt-Väisälä frequency can be written as

$$\omega_B^2 = -\frac{g}{\rho_0}\frac{d\rho_0}{dz} - \frac{g^2}{C^2}. \tag{3.15}$$

Substituting Equation 3.14 into Equation 3.15 and applying the quotient rule of differentiation leads to

$$\omega_B^2 = \frac{\gamma g}{\rho_0}\Big[\frac{1}{C^2}\frac{dp_0}{dz} + \frac{p_0}{C^4}\frac{dC^2}{dz}\Big] - \frac{g^2}{C^2}. \tag{3.16}$$

Since the atmosphere is assumed to be a perfect gas, substituting Equation 3.1 into the first term inside the square brackets, and considering Equation 3.14, Equation 3.16 becomes

$$\omega_B^2 = \frac{\gamma g R T}{C^2 H} + \frac{g}{C^2}\frac{dC^2}{dz} - \frac{g^2}{C^2}. \tag{3.17}$$

Grouping the terms and taking into account Equation 3.14 leads to the Brunt-Väisälä being written as

$$\omega_B^2 = \frac{(\gamma-1)g^2}{C^2} + \frac{g}{C^2}\frac{dC^2}{dz} = \omega_g^2 + \frac{g}{C^2}\frac{dC^2}{dz}, \tag{3.18}$$

ω_g is the isothermal Brunt-Väisälä frequency, which is the maximum possible frequency of the disturbed air parcel (Kohl *et al.*, 1996; Nappo, 2002). This oscillation of air in response to buoyancy is known as the atmospheric gravity wave (AGW) (Hines, 1960; Nappo, 2002).

3.3 Dispersion Relation for AGWs

During the passage of an AGW in a stable and motionless atmosphere, only the first order perturbation are considered. Therefore the velocity, pressure and density of the atmosphere in a perturbed state are given by

$$\mathbf{U} = \mathbf{U}_0 + \mathbf{U}_1, \tag{3.19}$$

$$p = p_0 + p_1, \tag{3.20}$$

and

$$\rho = \rho_0 + \rho_1, \tag{3.21}$$

respectively. $\mathbf{U}_0 = 0$, p_0 and ρ_0 are velocity, pressure and density at equilibrium. The parameters with subscript 1 represent the first-order perturbation of these parameters by the AGW (Beer, 1974). It is assumed that the perturbation each parameter $(p_1, \rho_1, U_{1x}, U_{1y}, U_{1z})$ is proportional to $e^{i(\omega t - K_x x - K_y y - K_z z)}$, i.e.

$$p_1, \rho_1, U_{1x}, U_{1y}, U_{1z} \propto e^{i(\omega t - K_x x - K_y y - K_z z)}, \tag{3.22}$$

where U_{1x}, U_{1y} are horizontal velocity components, U_{1z} is the vertical velocity component of the perturbation, and ω is the AGW frequency. The horizontal (K_x and K_y) and vertical (K_z) wave numbers are of complex form; this implies that the wave can undergo attenuation or amplification (Hines, 1960; Beer, 1974). For a two dimensional wave, U_{1y} and K_y are set to zero (Beer, 1974; Kelly, 2009). Furthermore, any movement of air is considered to be adiabatic. The Coriolis force has no effect on the motion, since gravity wave periods are less than 4 hours (Beer, 1974). Taking these assumptions into account, the equations of mass continuity, motion and adiabatic (Hines, 1960;

Beer, 1974; Nappo, 2002) become

$$\frac{\partial(\rho_1)}{\partial t} + \mathbf{U}_1 \cdot \nabla\rho_0 + \rho_0\nabla \cdot \mathbf{U}_1 = 0 \tag{3.23}$$

$$\rho_0\frac{\partial U_{1x}}{\partial t} + \frac{\partial p_1}{\partial x} = 0 \tag{3.24}$$

$$\rho_0\frac{\partial U_{1z}}{\partial t} + \frac{\partial p_1}{\partial z} + \rho_1 g = 0 \tag{3.25}$$

$$\frac{\partial(p_1)}{\partial t} + \mathbf{U}_1 \cdot \nabla p_0 - C^2\frac{\partial(\rho_1)}{\partial t} - C^2\mathbf{U}_1 \cdot \nabla\rho_0 = 0 \tag{3.26}$$

Taking into account that ρ_0 is given by Equation 3.6, and substituting Equation 3.22 into Equation 3.23 the result is

$$i\omega\rho_1 - \frac{U_{1z}\rho_0}{H} - \rho_0 iK_zU_{1z} - \rho_0 iK_xU_{1x} = 0. \tag{3.27}$$

Dividing Equation 3.27 by ρ_0, and rearranging the term leads to

$$i\omega\frac{\rho_1}{\rho_0} - iK_xU_{1x} + \Big(-\frac{1}{H} - iK_z\Big)U_{1z} = 0, \tag{3.28}$$

Substituting

$$p_1 = p_0e^{i(\omega t - K_xx - K_yy - K_zz)} \tag{3.29}$$

into Equation 3.24 leads to

$$\rho_0 i\omega aU_{1x} - ip_0K_xe^{i(\omega t - K_xx - K_yy - K_zz)} = 0. \tag{3.30}$$

Multiplying Equation 3.30 by $1/\rho_0$ and considering Equation 3.14, Equation 3.30 can be written as

$$\frac{-iK_xC^2}{\gamma}e^{i(\omega t - K_xx - K_yy - K_zz)} + i\omega U_{1x} = 0. \tag{3.31}$$

Since

$$\frac{p_1}{p_0} = e^{i(\omega t - K_xx - K_yy - K_zz)}, \tag{3.32}$$

then Equation 3.31 becomes

$$i\omega U_{1x} - \frac{iK_x C^2}{\gamma}\frac{p_1}{p_0} = 0 \tag{3.33}$$

Substituting Equation 3.29 into Equation 3.25 leads to

$$\rho_0 i\omega U_z - iK_z p_0 e^{i(\omega t - K_x x - K_y y - K_z z)} + e^{i(\omega t - K_x x - K_y y - K_z z)}\frac{\partial p_0}{\partial z} + g\rho_1 = 0. \tag{3.34}$$

Substituting Equation 3.14 for p_0 in the third term of Equation 3.34, considering Equation 3.6, and dividing Equation 3.34 by ρ_0 leads to

$$i\omega U_z - \frac{iK_z C^2}{\gamma}e^{i(\omega t - K_x x - K_y y - K_z z)} - \frac{C^2}{H\gamma}e^{i(\omega t - K_x x - K_y y - K_z z)} + g\rho_1 = 0. \tag{3.35}$$

Using Equation 3.32 and rearranging the terms leads to

$$g\rho_1 - \frac{C^2(1/H + iK_z)}{\gamma}\frac{p_1}{p_0} + i\omega U_z = 0. \tag{3.36}$$

Equation 3.26 becomes

$$i\omega p_1 - \frac{RTU_{1z}\rho_0}{H} - iC^2\omega\rho_1 + \frac{C^2 U_{1z}\rho_0}{H} = 0, \tag{3.37}$$

rearranging this equation, and considering the definition of H from Section 3.1, Equation 3.37 becomes

$$-iC^2\omega\rho_1 + i\omega p_1 + (\gamma g\rho_0 - g\rho_0)U_{1z} = 0. \tag{3.38}$$

Substituting Equation 3.29 into the second term, Equation 3.38 becomes

$$-iC^2\omega\rho_1 + i\omega p_0 e^{i(\omega t - K_x x - K_y y - K_z z)} + (\gamma g\rho_0 - g\rho_0)U_{1z} = 0, \tag{3.39}$$

diving by $1/\rho_0$, and considering Equation 3.32 the adiabatic state equation becomes

$$-i\omega C^2\frac{\rho_1}{\rho_0} + \frac{i\omega C^2}{\gamma}\frac{p_1}{p_0} + (\gamma - 1)gU_{1z} = 0, \tag{3.40}$$

respectively. Defining the vector,

$$\mathbf{F} = \begin{bmatrix} \rho_1/\rho_0 \\ p_1/p_0 \\ Ux \\ Uz \end{bmatrix}, \tag{3.41}$$

the continuity, motion, and adiabatic state equations (Equation 3.28, 3.33, 3.36 and 3.40) can be written as

$$\begin{bmatrix} i\omega & 0 & -iK_x & -\frac{1}{H} - iK_z \\ 0 & -iK_xC^2/\gamma & i\omega & 0 \\ g & -C^2(1/H + iK_z)/\gamma & 0 & i\omega \\ -i\omega C^2 & i\omega C^2/\gamma & 0 & (\gamma-1)g \end{bmatrix} \begin{bmatrix} \rho_1/\rho_0 \\ p_1/p_0 \\ Ux \\ Uz \end{bmatrix} = \mathbf{0}. \tag{3.42}$$

The solution of Equation 3.42 is non-trivial (non-zero) if the determinant of the 4×4 matrix is zero (Beer, 1974). This means that

$$\omega^4 - \omega^2 C^2 (K_x^2 + K_z^2) + (\gamma - 1) g^2 K_x^2 + i\gamma\omega^2 K_z = 0. \tag{3.43}$$

Assuming that the wave amplitude does not change in the horizontal direction leads to $K_x = k_x$, where k_x is real. Let the vertical amplitude be subjected to attenuation or growth, then $K_z = k_z + ik_z'$, where k_z and k_z' are real. This means that Equation 3.43 is complex, with the real part being

$$\omega^4 - \omega^2 C^2 (k_x^2 + k_z^2 - k_z'^2) - \omega^2\gamma g k_z' + (\gamma - 1) g^2 k_x^2 = 0, \tag{3.44}$$

and the imaginary part being

$$\omega^2 \gamma g k_z - 2\omega^2 C^2 k_z k_z' = 0. \tag{3.45}$$

Equation 3.45 holds if

$$\omega = 0, \tag{3.46}$$

$$k_z = 0, \tag{3.47}$$

or

$$k'_z = \frac{\gamma g}{2C^2}. \tag{3.48}$$

The latter condition is the desired one since Equation 3.46 implies that there is no wave; Equation 3.47 suggests that the wave only propagates horizontally, without being dissipated. Substituting Equation 3.48 into Equation 3.44 leads to

$$\omega^4 - \omega^2 C^2 (k_x^2 + k_z^2) + (\gamma - 1) g^2 k_x^2 - \omega^2 g^2 \gamma^2 / 4C^2 = 0. \tag{3.49}$$

Equation 3.49 is the same dispersion relation for AGWs as the one given by Hines (1960). Making k_z the subject, Equation 3.49 can be written as

$$k_z^2 = \Big(\frac{\omega_g^2 - \omega^2}{\omega^2}\Big) k_x^2 + \frac{\omega^2 - \omega_a^2}{C^2}; \tag{3.50}$$

ω_g was introduced in Equation 3.18, and

$$\omega_a = \frac{\gamma g}{2C} \tag{3.51}$$

is the minimum frequency for sound waves. Since k_z is real, $\omega_g < \omega < \omega_a$ implies that the AGWs is an evanescent wave, i.e., the wave dissipates exponentially. As a result, an AGW can exist in either high ($\omega > \omega_a$) or low ($\omega < \omega_g$) frequency mode. For high frequencies, Equation 3.50 approximates to

$$k_z^2 + k_x^2 \approx \frac{\omega^2}{C^2}, \tag{3.52}$$

which means that the wave is simply a sound wave. In the atmosphere sound waves have periods less than 4 minutes (Beer, 1974). At low frequencies

Equation 3.50 approximates to

$$k_z^2 \approx \frac{\omega_g k_x^2}{\omega^2} - \frac{\omega_a}{C^2}. \tag{3.53}$$

This represents the propagation of a wave under the influence of gravity (AGW). In the atmosphere AGWs propagate with periods between 4 minutes and 3 hours (Beer, 1974).

3.4 Sources of AGWs

AGWs are generated when atmosphere is perturbed by different kinds of atmospheric processes: the passage of a solar terminator (Somsikov and Troitskiy, 1975), the occurrence of magnetic storms (Thome, 1968) and meteorological process in the lower atmosphere (Yeh, 1972). There are other source mechanisms that lead to generation of AGWs, namely solar eclipse (Chimonas, 1970b), nuclear explosions (Row, 1967) and large earthquakes (Artru *et al.*, 2005); however, these are outside the scope of this thesis and will not be discussed.

The solar terminator, i.e. boundary region that separates daytime and nighttime on Earth, is characterized by abrupt changes in atmospheric parameters, namely temperature and pressure (Somsikov and Ganguly, 1991). Furthermore, Somsikov and Ganguly (1991) stated that these sudden changes result in pressure instabilities. As a result, the reaction of gravity to these disturbances will cause AGWs that travel in the same direction (more or less westward) as the solar terminator (Somsikov and Troitskiy, 1975).

As discussed in Section 2.3.4, magnetic storms are accompanied by injection of highly energetic particles into the ionosphere. These particles enter the ionosphere in the high latitude regions, and penetrate down to the neutral atmosphere, where they transfer their energy in a form of heat. In response to this process, the neutral atmosphere expands and bulges, implying that heat has been converted to gravitational potential energy. When the Earth's gravity acts in order to restore equilibrium in the atmosphere, equatorward traveling AGWs will be generated (Thome, 1968; Hernandez and Roble, 1978).

Chimonas (1970a) showed that the Lorentz force (due to equatorial electrojet) on ions can be enhanced during magnetic storms, such that it leads to stronger coupling between ions and neutral particles at geomagnetic equator. Through this coupling, ions transfer energy to the neutral particles, resulting in generation of poleward traveling AGWs (Chimonas, 1970a).

Localized heating in the troposphere reduces the density of the heated air parcel. The warmer air will rise as a plume until it reaches the stable stratosphere. A bulge will occur on the bottom stratosphere if the plume's energy is converted into gravitation potential energy. If the bulge is about 1 to 3 km, an AGW wave will be formed when the Earth's gravity acts to restore equilibrium (Vadas and Lui, 2009).

When wind blows over a mountain, the mountain acts as a barrier and instabilities occur on the lee side, creating turbulence. The act of gravity results in AGWs terms mountain waves (Fritts and Alexander, 2003; Van Der Mescht, 2012).

3.5 Modes of AGWs Propagation

Mayr *et al.* (1991) showed that there are four possible modes (modes 1, 2, 3 and 4) that an AGW can assume as it propagates in the atmosphere, depending on its magnitude and source. These modes are depicted in Figure 3.1. AGWs in a direct mode (1) propagate nearly horizontally in the thermosphere. Such waves travel great distances at high speeds, and they have long wavelengths; moreover they are confined to travel in the upper atmosphere. Hocke and Schlegel (1996) stated that these waves appear to be traveling equatorward; which means that they correspond to those that originate at high latitudes at the onset of magnetic storms. AGWs in mode 2, are generated in the lower thermosphere, they travel at oblique angles relative to the Earth's surface. Moreover, waves in mode 2 have shorter wavelengths, as a result they experience attenuation as they travel upward. This is due to high viscosity and thermal conduction at higher atmospheric regions (Hines, 1965; Kohl *et al.*, 1996).

Similar to those in mode 2, AGWs in lower modes (3 and 4) also travel at lower speeds, and they have shorter wavelengths. These types of waves are hardly related to a specific atmospheric process, as they occur randomly (Beer, 1974; Hajkowicz, 1990; Samuel, 1974). Mode 3 depicts a wave that propagates between the Earth's surface and the lower thermosphere. This wave is able to propagate long distances because there is less viscosity and thermal conduction in the lower atmosphere. However, the wave can leak into the upper atmosphere, as in shown in the Figure 3.1. Mode 4 depicts waves that are reflected on the Earth's surface and propagate into the thermosphere.

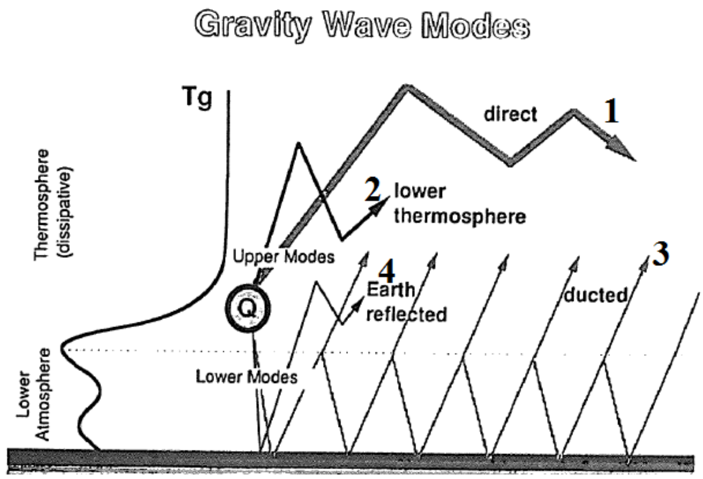

Figure 3.1: AGW modes in the lower and upper atmosphere (Mayr *et al.*, 1991).

3.6 Ionospheric Response to Gravity Waves

As an AGW propagates into higher altitudes it transfers its energy to fewer molecules (McNamara, 1991), as a result its amplitude increases with height (Hines, 1965). However at higher altitude the AGWs experience energy dissipation. Consequently, AGWs of shorter wavelengths are attenuated at altitudes of about 110 to 120 km, while those with longer wavelengths persist to greater altitudes (Hines, 1960).

At ionospheric heights AGWs collide with the plasma and set the ions into motion. In lower ionosphere (mainly in the D region), the collision results into ion density perturbations similar to that of neutral particles. Electron density also follows the same behavior since electrons are attracted to ions by electrostatic forces (Rawer, 1993). Essentially, in the lower ionosphere, plasma motions are the same as that of neutral atmosphere.

In the upper ionosphere the geomagnetic field modifies the plasma motions, such that they differ from that of neutral particles (Rawer, 1993). In the F2 layer these motions are more or less aligned to the geomagnetic field (Beer, 1974; Rawer, 1993). In order to derive ionospheric perturbations, it is necessary to state the continuity equation for electron which is given by

$$\frac{dN_e}{dt} + \nabla \cdot (N_e \mathbf{v}_e) = P - L, \tag{3.54}$$

where P and L are electron production and loss rates as defined in Section 2.1, $\mathbf{v}_e$ is the electron velocity (Ratcliffe, 1960; Hargreaves, 1979; Ondoh and Marubashi, 2000). The passage of a gravity wave will disturb the electron density, which will split into two: the background N_{e0}, and the perturbed N'_e electron density such that $N_e = N_{e0} + N_{e1}$. Similarly the electron velocity is given by $\mathbf{v}_e = \mathbf{v}_{e0} + \mathbf{v}_{e1}$. It is assumed that there are no electrons produced or lost, and $\mathbf{v}_{e0} = 0$ (Hooke, 1970), therefore Equation 3.54 becomes

$$\frac{dN_{e1}}{dt} = -\nabla \cdot (N_{e0} \mathbf{v}_{e1}). \tag{3.55}$$

The equation of motion for an electron is

$$m_e \frac{d\mathbf{v}_{e1}}{dt} = \mathbf{F}_g + \mathbf{F}_p + \mathbf{F}_C + \mathbf{F}_m + \mathbf{F}_f, \tag{3.56}$$

where m_e is the electron mass, $\mathbf{F}_g$ is the force of gravity, $\mathbf{F}_p$ is the pressure gradient force, $\mathbf{F}_C$ is the Coriolis force, $\mathbf{F}_m$ is the Lorentz force, and $\mathbf{F}_f$ is the frictional force due to electrons colliding with other particles. Some of these forces (the pressure gradient force, gravity and the Coriolis force) are insignificant compared to the geomagnetic force; hence they may be ignored. Furthermore, only the frictional force due to electron-neutral collision may be taken into account (Beer, 1974; Kelly, 2009). This reduces Equation 3.56 to

$$e^{-}(\mathbf{v}_{e1} \times \mathbf{B}) + m_e \nu_n (\mathbf{v}_{e1} - \mathbf{U}_1) = 0, \tag{3.57}$$

where the first term on the left represents the Lorentz force. The second and third terms are friction due to the collision of electrons and neutral particles, respectively. The parameters in Equation 3.57 are defined as follows:

- $\mathbf{B}$ is the geomagnetic filed,
- m_e is the electron mass,
- and ν_n is the electron-neutral collision frequency.

The solution to Equation 3.57 is given by MacLeaod (1966) as

$$\mathbf{v}_{e1} = \frac{1}{1+r^2}[r^2\mathbf{U}_1 + r(\mathbf{U}_1 \times \mathbf{1_b}) + (\mathbf{U}_1 \times \mathbf{1_b})\mathbf{1_b}], \tag{3.58}$$

where r is the ratio of ion-neutral frequency to the electron gyrofrequency, $\mathbf{1_b}$ is a unit vector in the direction of the geomagnetic field. MacLeaod (1966) further stated that at altitudes greater than 170 km $r << 1$, which leads to

$$\mathbf{v}_{e1} \approx (\mathbf{U}_1 \cdot \mathbf{1_b})\mathbf{1_b}. \tag{3.59}$$

Assuming that the perturbed electron density is of the form

$$N_{e1} \propto e^{i(\omega t + k_x x + k_y y)} \tag{3.60}$$

(Hooke, 1970), the perturbed electron density in Equation 3.55 becomes

$$N_{e1} = -\frac{1}{i\omega}\nabla \cdot [N_{e0}(\mathbf{U}_1 \cdot \mathbf{1_b})\mathbf{1_b}]. \tag{3.61}$$

It can be seen from Equation 3.61 that these AGW induced electron density fluctuations propagate in space; they are referred to as traveling ionospheric disturbance (TIDs) (Hines, 1963; Rawer, 1993).

3.7 Traveling Ionospheric Disturbances and their Characteristics

TIDs are mainly classified into two categories: medium scale TIDs (MSTIDs) and large scale TIDs (LSTIDs) (Beer, 1974). The review of TIDs in this section will be on studies conducted in areas which are more or less on the same geomagnetic latitude as South Africa. This is due to the influence of the geomagnetic field on TIDs. From hereon, seasons will be those of the Southern Hemisphere.

3.7.1 Medium Scale TIDs

MSTIDs propagate at velocities between 50 and 300 m/s with periods less than an hour (Hernández-Pajares *et al.*, 2012). MSTIDs occur more frequently compared to LSTIDs (Beer, 1974; Hajkowicz, 1990). They are manifestations of AGWs in mode 2, 3, and 4. Hence they are difficult to predict, because they are hardly related to a specific event (Hocke and Schlegel, 1996), except those that are generated by the passage of the solar terminator (e.g. Afraimovich, E. F. and Edemskiy, I. K. and Leonovich, A. S. and Leonovich, L. A. and Voeykov, S. V, 2009).

The first comprehensive study of TIDs in South Africa was conducted by Chum *et al.* (2012). They performed their investigation using Doppler sounding systems on a year long period from June 2010. They found that MSTIDs propagate poleward in summer, and equatorward during winter. These findings seem to agree with Munro (1958) who found that in winter, MSTIDs propagate in the azimuth of 30° (north being 0°). Furthermore, in summer MSTIDs propagate in the azimuth of 120°.

Chum *et al.* (2012) found that MSTIDs have higher velocities in winter as opposed to summer (on average 100 m/s in summer, and 125-150 m/s in winter.) Although they stated that differences were within the velocities error ranges, the trend agrees with Tyalimpi (2014). Furthermore, Munro (1958) found a similar trend with maximum velocity of 150 m/s in winter.

Sindelarova *et al.* (2012) concluded that MSTIDs (with period less than 30 minutes) are independent of geomagnetic activity. They observed that MSTIDs of periods between 30 to 50 minutes seem to occur more frequently during moderate magnetic storms. Moreover, Ding *et al.* (2014), in their comprehensive performed in China, found that the number of MSTIDs increases with geomagnetic activity; and their most preferred direction is equatorward. Tyalimpi (2014) also found similar results regarding MSTIDs in South Africa.

3.7.2 Large Scale TIDs

LSTIDs propagate with velocities between 300 and 1000 m/s with periods between 0.5 to 3 h (Crowley and Rodrigues, 2012). LSTIDs are generated when AGWs in mode 1 excite the ionosphere (Hocke and Schlegel, 1996). For many years it was accepted that LSTIDs are caused by AGWs that propagate equatorward at the onset of magnetic storms (Thome, 1968; Hernandez and Roble, 1978; Hajkowicz, 1990; Hocke and Schlegel, 1996). Some of these TIDs propagate across the equator and appear as poleward TIDs on the opposite Hemisphere (Ding *et al.*, 2013). Recently it has been shown that not all poleward TIDs are those which cross the equator. Habarulema *et al.* (2015) reported poleward LSTIDs during magnetic storms; they stated that the TIDs were not those which travel across the equator. They associated the

TIDs to equatorial electrodynamic processes described by Chimonas (1970a) (see Section 3.4). There exists other poleward LSTIDs which are not related to any geomagnetic activities; these propagate over smaller latitudinal ranges (Ding *et al.*, 2013). Vadas and Lui (2009) suggested that they could be induced by large AGW (propagating at about 480 to 510 m/s) which originate as secondary waves when smaller AGWs dissipate in the thermosphere.

3.8 The Importance of Studying TIDs

The ionosphere is an important medium of propagation for HF communication, and GPS positioning radio waves (McNamara, 1991; Lastovicka *et al.*, 2004). As discussed in Section 1.1, the passing of TIDs changes the structure of the ionosphere, and subsequently its refraction index. Consequently, undesirable delays in the trans-ionospheric in GPS, and reflected HF communication signals may occur. According to Klobuchar (1986) these delays can lead to uncertainties of about 15 meters in GPS positioning. Therefore, studying TIDs may be beneficial in compensating for these uncertainties (Lastovicka *et al.*, 2004). Furthermore, an understating of TIDs is important in HF communication so that accurate reflection angles may be used when transmitting HF waves(Lastovicka *et al.*, 2004).

Chapter 4

Data and Methodology

This chapter provides an introduction to GPS and its segments. The definition of vertical total electron content is provided, followed by the discussion on how it was used to study TIDs. Finally, the methods used to determine periods and velocities of TIDs are also discussed.

4.1 GPS Overview

GPS was established by the U. S. Department of Defence (DoD) (Hofmann-Wellenhof *et al.*, 1992). It is the most prevelent member of a large constellation of satellites known as the global navigation satellite system (GNSS). Currently the other satllite systems associated with GNSS are BeiDou, Galileo, GLANOSS, Navigation Indian Constellation and Quasi-Zenith (gps.gov, 2017c). The aim of GNSS is estimating parameters such as position, velocity and time (Misra and Enge, 2006).

The GPS estimates these parameters using radio signals from satellites that orbit the Earth at about 20 000 km altitude (Hofmann-Wellenhof *et al.*, 1992). The DoD provides two access methods for GPS usage: the standard positioning service (SPS), and the precise positioning service (PPS). The SPS is available for civilian users, however, the PPS is restricted to authorized DoD users (Misra and Enge, 2006). The functions of GPS are performed by three segments: space, control, and user (Hofmann-Wellenhof *et al.*, 1992).

4.1.1 The Space Segment

The space segment is made up of at least 24 satellites, each orbiting the Earth every 12 hours (Misra and Enge, 2006). The satellites transmit signals on three frequencies: L1 = 1575.42 MHz, L2 = 1227.60 MHz and L5 = 1176.45 MHz. These frequencies are obtained by multiplying the fundamental L-band frequency of 10.23 MHz by 154, 120, and 115, respectively (Misra and Enge, 2006). Each signal contains a carrier, ranging code, and the navigation data. A carrier is a sinusoidal signal with a frequency of either L1, L2 or L5 (Misra and Enge, 2006). The ranging code is a group of codes that are normally referred to as pseudo-random noise (PRN) codes; they enable satellites to transmit the same frequencies without interfering with each other (Misra and Enge, 2006). PRN codes that are associated with SPS are known as coarse/acquisition (C/A) codes; those that are transmitted on PPS are referred to as precision (P(Y)) codes (Misra and Enge, 2006). The navigation data is a message that contains information about the satellite's position, velocity, health status, and clock bias parameters (Misra and Enge, 2006; Hofmann-Wellenhof *et al.*, 1992). Each satellite is equipped with four atomic clocks on board, and it continuously broadcasts radio signals that are marked with their transmission time (Ferguson, 1997).

4.1.2 Control Segment

The control segment consists of a global network of ground base control stations. The main control station (Master Control Station) is located at the U.S. Air Force Base in Colorado (Misra and Enge, 2006; gps.gov, 2017b). The control segment is responsible for tracking, and updating navigation messages of satellites (Ferguson, 1997). Furthermore, it predicts clock parameter, velocity and position of the satellites; and it maintains the satellites' health (Hofmann-Wellenhof *et al.*, 1992; Misra and Enge, 2006).

4.1.3 User Segment

The user segment consists of devices that are able to receive GPS signals. These receivers are equipped with clocks which are synchronized with satellite clocks. At any given time each receiver generates a reference signal similar to the one that it receives from the satellite. In order to determine the receiver-satellite range, the receiver compares the reference with the satellite-generated signal. This can be performed in two ways: by multiplying the received signal's transit time by the speed of light, or taking the phase difference between the reference and the received signal (Hofmann-Wellenhof *et al.*, 1992). However, due to imperfect synchronization of receiver and satellite clocks, the range is referred to pseudorange (Misra and Enge, 2006).

4.1.4 Code Pseudorange

A signal transmitted at time t_s according to satellite clock (where t_s is encoded in the PRN codes), will be received at time t_r according to receiver clock. Due to transmission and reception delays, t_s and t_r will have errors δt_s and δt_r associated with them (Hofmann-Wellenhof *et al.*, 1992). Therefore, transit time for the signal is given by

$$\Delta t = \Delta t_{GPS} + \Delta\delta t_{GPS}, \tag{4.1}$$

where $\Delta t_{GPS} = t_r - t_s$, and $\Delta\delta t_{GPS} = \delta t_r - \delta t_s$. Multiplying Equation 4.1 by the speed of light ($c = 3 \times 10^8$ m/s) results in a code derived pseudorange (R_{pseudo}):

$$R_{pseudo} = c\Delta t = \varrho + c\Delta\delta t_{GPS}, \tag{4.2}$$

where $\varrho = c\Delta t_{GPS}$.

4.1.5 Carrier Phase Pseudorange

The pseudorange can also be determined through carrier phase measurements. This is done by determining the carrier beat, i.e. the difference between the phase of the reference and the received signal (Misra and Enge, 2006). The phase of the satellite signal (φ_s) is given by

$$\varphi_s(t) = \xi_s t - \xi_s \frac{\varrho}{c} - \varphi_{s0}, \tag{4.3}$$

with

$$\varphi_{s0} = \xi_s \delta t_s \tag{4.4}$$

where time t is in GPS time, ξ_s is the frequency of the signal, $c \approx 3 \times 10^8$ m/s is the speed of light, and φ_{s0} is the initial phase where $t = 0$ (Hofmann-Wellenhof *et al.*, 1992). The phase of the reference signal is

$$\varphi_r(t) = \xi_r t + \varphi_{r0}, \tag{4.5}$$

with

$$\varphi_{r0} = \xi_r \delta t_r \tag{4.6}$$

where ξ_r is the frequency of the reference signal, and φ_{r0} is the phase at $t = 0$ (Hofmann-Wellenhof *et al.*, 1992). The carrier beat becomes

$$\varphi_{sr} = \varphi_s(t) - \varphi_r(t) = -\xi_s \frac{\varrho}{c} - \xi_s \delta t_s + \xi_r \delta t_r + (\xi_s - \xi_r)t. \tag{4.7}$$

According to Hofmann-Wellenhof *et al.* (1992) the deviation of ξ_s and ξ_r from the mean frequency (ξ) is insignificant, therefore substituting ξ_m for ξ_s and ξ_r Equation 4.7 reduces to

$$\varphi_{sr} = -\xi_m \frac{\varphi}{c} - \xi_m \mathit{\Delta} \delta t_{GPS} \tag{4.8}$$

When a phase beat measurement is made by a receiver, the number of carrier cycles (J) between the satellite and the receiver is unknown. This introduces an ambiguity in the phase measurement, hence the phase beat is given by

$$\varphi_{sr} = \mathit{\Delta}\varphi_{sr} + J, \tag{4.9}$$

where $\mathit{\Delta}\varphi_{sr}$ is the phase measured by the receiver (Hofmann-Wellenhof *et al.*, 1992). Substituting Equation 4.8 into Equation 4.9 and noting that

$$\xi = \frac{c}{\lambda}, \tag{4.10}$$

where λ is the wavelength, leads to

$$\sigma = -\mathit{\Delta}\varphi_{sr} = \frac{1}{\lambda}\varrho + \frac{c}{\lambda}\mathit{\Delta} t_{GPS} + J. \tag{4.11}$$

It can be seen that multiplying Equation 4.11 by λ results in pseudorange.

4.2 Ionospheric Effect on GPS

A signal transmitted from a satellite travels at a constant speed of light, c, until it encounters the Earth's ionosphere where it gets refracted (Misra and

Enge, 2006). The refraction changes the velocity of the signal, which causes transit time delay. Consequently, the measured pseudorange will have an error, which is referred to as ionospheric refraction (I_ξ) (Hofmann-Wellenhof *et al.*, 1992); measured in meters, and is given by

$$I_\xi = \frac{40.3}{\xi} \int N_e ds, \tag{4.12}$$

where N_e is the electron density as defined in Section 2.2, ds is a differential distance along the line on travel, and

$$\text{TEC} = \int N_e ds. \tag{4.13}$$

TEC is known as the total electron content, i.e total number of electrons the signal encounters along its propagation path (Klobuchar, 1986; Hofmann-Wellenhof *et al.*, 1992). When the satellite is at zero zenith (relative to the receiver), the TEC is known as vertical TEC (VTEC). However, when the zenith is greater than zero, the TEC is referred to as the slant TEC (STEC). The TEC is measured in units of total electron content units (TECU), where 1 TECU = 10^{16} e^-/m^2 (Misra and Enge, 2006). In addition to N_e, the TEC is also dependent on variations that were discussed in Section 2.3 (Klobuchar, 1986). If not corrected, during magnetic storms, the ionospheric refraction may result in positioning error of about 100 meters (Klobuchar, 1986).

4.2.1 Eliminating the Ionospheric Effect

Dual frequency receivers are able to use L1 and L2 to determine and remove most of the effect of TEC on the pseudoranges. This is achieved by measuring the difference between the delays of L1 and L2 (Fees and Stephens, 1986). Considering code derived pseudoranges, R_1 and R_2, obtained from L1 and L2, respectively and taking into account the ionospheric refractions, the pseudoranges become

$$R_1 = c\varDelta t = \varrho + c\varDelta\delta t_{GPS} + I_1, \tag{4.14}$$

and

$$R_2 = c\varDelta t = \varrho + c\varDelta\delta t_{GPS} + I_2. \tag{4.15}$$

where I_1 and I_2 are ionospheric refractions on L1 and L2. Taking the difference between R_2 and R_1, and considering Equation 4.12 leads to

$$R_2 - R_1 = 40.3\left[\frac{1}{\mathrm{L}_2^2} - \frac{1}{\mathrm{L}_1^2}\right]\mathrm{TEC}. \tag{4.16}$$

Making TEC the subject, Equation 4.16 becomes

$$\mathrm{TEC} = \frac{1}{40.3}\left[\frac{1}{\mathrm{L}_2^2} - \frac{1}{\mathrm{L}_1^2}\right]^{-1}(R_2 - R_1). \tag{4.17}$$

The TEC can also be obtained from carrier pseudoranges. Multiplying Equation 4.11 by λ, and taking into account the ionospheric delay leads to

$$\varPhi_1 = \lambda_1\sigma_1 = c\varDelta t = \varrho + c\varDelta\delta t_{GPS} + \lambda_1 J_1 + I_1, \tag{4.18}$$

and

$$\varPhi_2 = \lambda_2\sigma_2 = c\varDelta t = \varrho + c\varDelta\delta t_{GPS} + \lambda_2 J_2 + I_2, \tag{4.19}$$

where λ_1 and λ_1 are wavelengths of L1 and L2 signals. The difference between Equation 4.19 and 4.18 is

$$\varPhi_1 - \varPhi_2 = \lambda_1 J_1 + I_1 - (\lambda_2 J_2 + I_2) \tag{4.20}$$

Substituting Equation 4.12 into Equation 4.20, and solving for TEC leads to

$$\mathrm{TEC} = 9.52[(\varPhi_1 - \varPhi_2) - (\lambda_1 J_1 - \lambda_2 J_2)]. \tag{4.21}$$

Substituting Equation 4.17 or Equation 4.21 into Equation 4.12, the ionospheric effected can be corrected in pseudoranges.

4.3 Vertical Total Electron Content

For this project, observables (code and phase derived pseudoranges) were obtained from dual frequency (L1 and L2) receivers located in various places in South Africa. Figure 4.1 shows how the GPS receiver stations (marked with black tripod shapes) were distributed. Files (in receiver independent exchange format) containing observables at 30 seconds intervals for the year 2010 were obtained from the Trignet ftp site (ftp://ftp.trignet.co.za/). Software (GPS-TEC) developed at the Institute for Scientific Research in Boston College (Seemala, 2004) was used to determine TEC (defined by Equation 4.13) from the observation files. For every STEC value, GPS-TEC computes VTEC, i.e. a TEC value that would be obtained if a satellite was directly overhead a given geographic position. This is achieved by firstly assuming that the ionosphere is represented by a thin shell at about 350 km altitude, as shown in Figure 4.2 (Seemala, 2004; Klobuchar, 1986). The projected geographic position where the line of sight intercepts the shell is known as the ionospheric pierce point (IPP) (Hofmann-Wellenhof *et al.*, 1992).

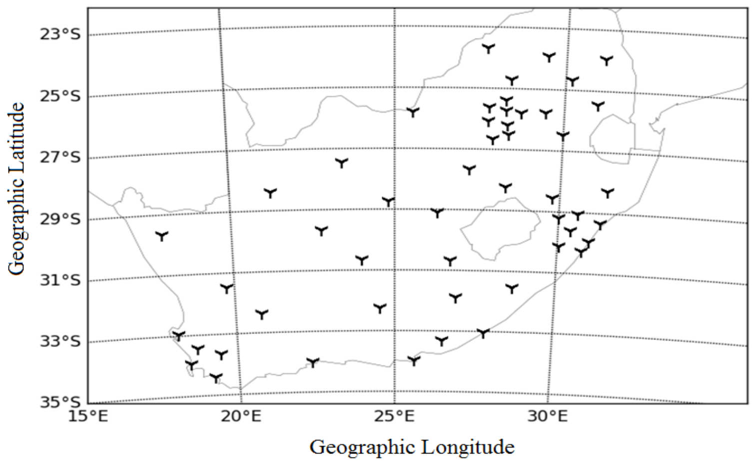

Figure 4.1: A geographical distribution of GPS receiver network (marked with black tripod shapes) where data were obtained for the year 2010.

In order to transform STEC to VTEC, GPS-TEC uses the following geometric relation from Figure 4.2:

$$\mathrm{VTEC} = \frac{\mathrm{STEC}}{S(\mathrm{E})} \tag{4.22}$$

where the projection angle $S(E)$ is given by

$$S(\mathrm{E}) = \frac{1}{\cos z} = \left[1 - \left(\frac{\mathrm{R}_E \cos(\mathrm{E})}{\mathrm{R}_E + \mathrm{h}_m}\right)^2\right]^{-0.5}. \tag{4.23}$$

The elevation angle (E) is the angle between the horizontal and the line of sight, z is the angle between the line of sight and the vertical, $\mathrm{R}_E = 6371$ km is the radius of the Earth, and h_m is the altitude of the ionospheric shell (Hofmann-Wellenhof *et al.*, 1992).

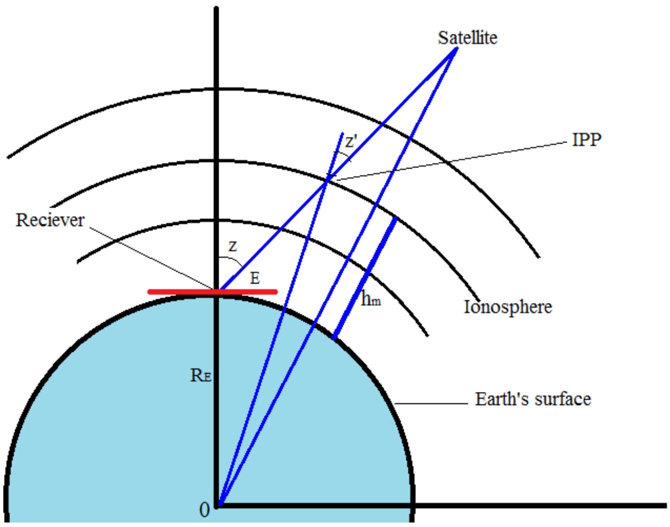

Figure 4.2: Geometry of the signal path from satellite to receiver (Hofmann-Wellenhof *et al.*, 1992).

4.3.1 Detrending VTEC

VTEC measurements from GPS receivers contain diurnal trend. This can be seen from Figure 4.3 where the VTEC was measured by a receiver station

ANTH (located at 30°S and 26.56°E) on 2010-01-01. This date was chosen randomly to show a typical diurnal TEC variation (magnetic conditions quiet with minimum of -1 nT; maximum Kp index of 1) and to illustrate how data processing in order to identify TID features was done. In order to filter out the multipath effects, data from satellites below the elevation angle of 35° were removed. To identify any other features in VTEC measurements, the diurnal trend (as a dominant feature) was removed using 6^{th} order polynomials (Zhou *et al.*, 2017). Figure 4.4A shows an example of the polynomial fitting to VTEC measurements from one GPS satellite (PRN 24). The filtered VTEC time series (shown in Figure 4.4B), denoted by dTEC, was obtained by subtracting the polynomial fitted TEC from the corresponding VTEC time series. The presence of wave (periodic oscillations) structures can clearly be seen from 17 to 19.5 hours in Figure 4.4A and Figure 4.4B.

4.3.2 dTEC Maps

Maps of the detrended VTEC, i.e. dTEC were created in order to depict the waves structures that appeared in TEC data. The maps were defined by a grid of 0.5 °× 0.5 ° pixel resolution with dimensions: 20 ° - 35 °S , and 15 ° - 35 °E. This resulted in an image with 30 × 40 pixels. It can be seen from Figure 4.1 that this area contains all the receiver stations. In order to create a dTEC map at a given time, the values of dTEC of each pixel were averages of dTEC whose IPPs were ±0.5° from each pixel. Wave structures were identified as peaks and troughs in the dTEC maps. If wave structures observed from dTEC maps were propagating in time, i.e. they represented TIDs, the peaks and troughs appeared to be propagating on successive maps. An example of such dTEC maps is shown in Figure 4.5, where a dTEC enhancement can be seen propagating from nearly South-

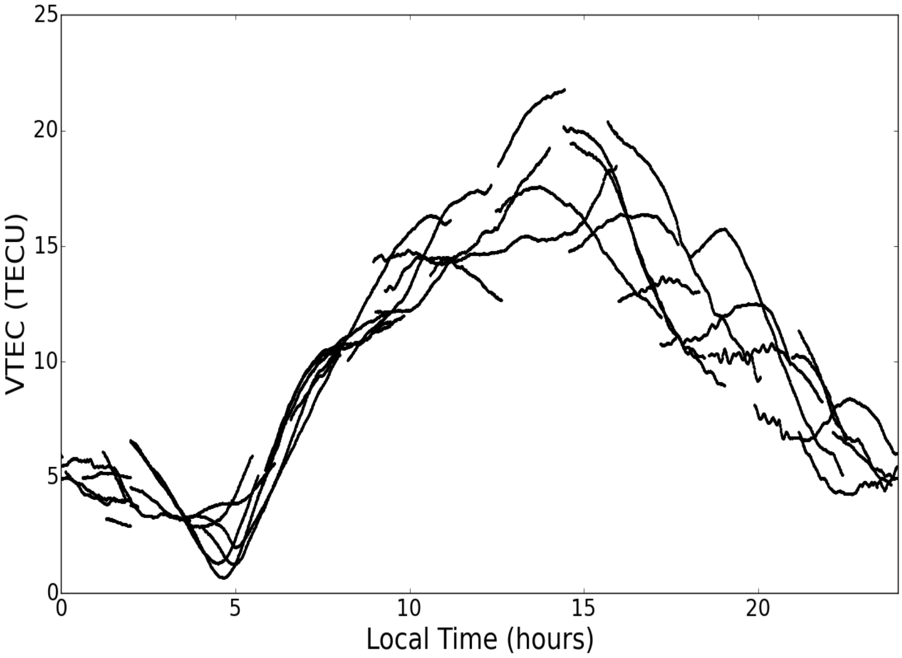

Figure 4.3: VTEC measurements taken at ANTH (30°S, 26.56°E) on 2010-01-01.

West to North-East.

4.4 Methodology

The were two methodologies that were applied to determine propagation parameters of TIDs: the continuous wavelet transform was used to determine periods, and the particle image velocimetry was applied in determining velocities.

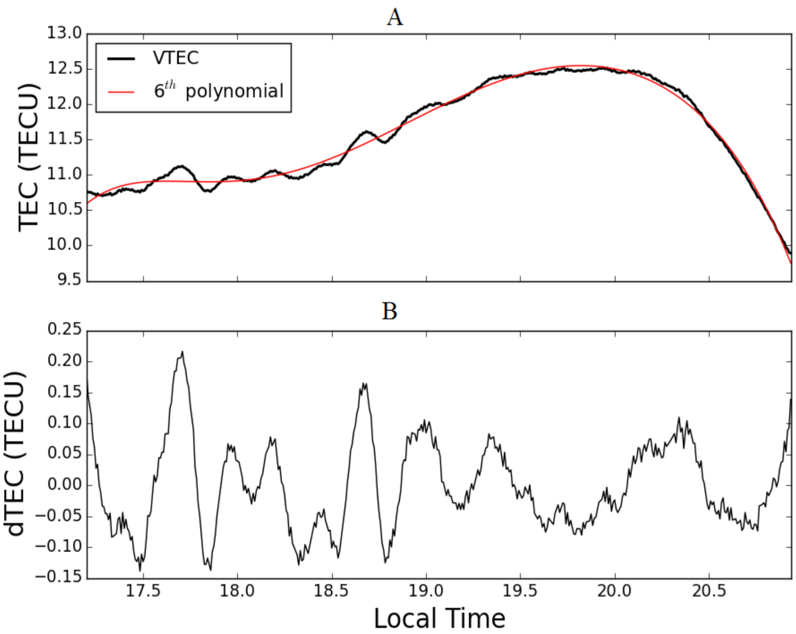

Figure 4.4: VTEC time series for PRN 7 measured at ANTH on 2010-01-01 fitted with a 6^{th} order polynomial (A), and the detrended VTEC (B).

4.4.1 Continuous Wavelet Analysis

Continuous Wavelet transform (CWT) is a method used to decompose a time series into frequency-time space. This is done by convolving the time series with a scaled wavelet (Torrence and Compo, 1998). A wavelet ($\psi(t)$), either real or complex, is a function that satisfies

$$\int_{-\infty}^{\infty} \psi(t) = 0, \tag{4.24}$$

and is localized in time and frequency (Farge, 1992). Such a wavelet is known as mother wavelet; it can be dilated (stretched or shrunken) and translated in time (Torrence and Compo, 1998). The parameters responsible for dilation and translation (denoted s and τ) transform $\psi(t)$ to $\psi_{s,\tau}(t)$ by:

$$\psi_{s,\tau}(t) = \frac{1}{\sqrt{s}}\psi\Big(\frac{t-\tau}{s}\Big), \tag{4.25}$$

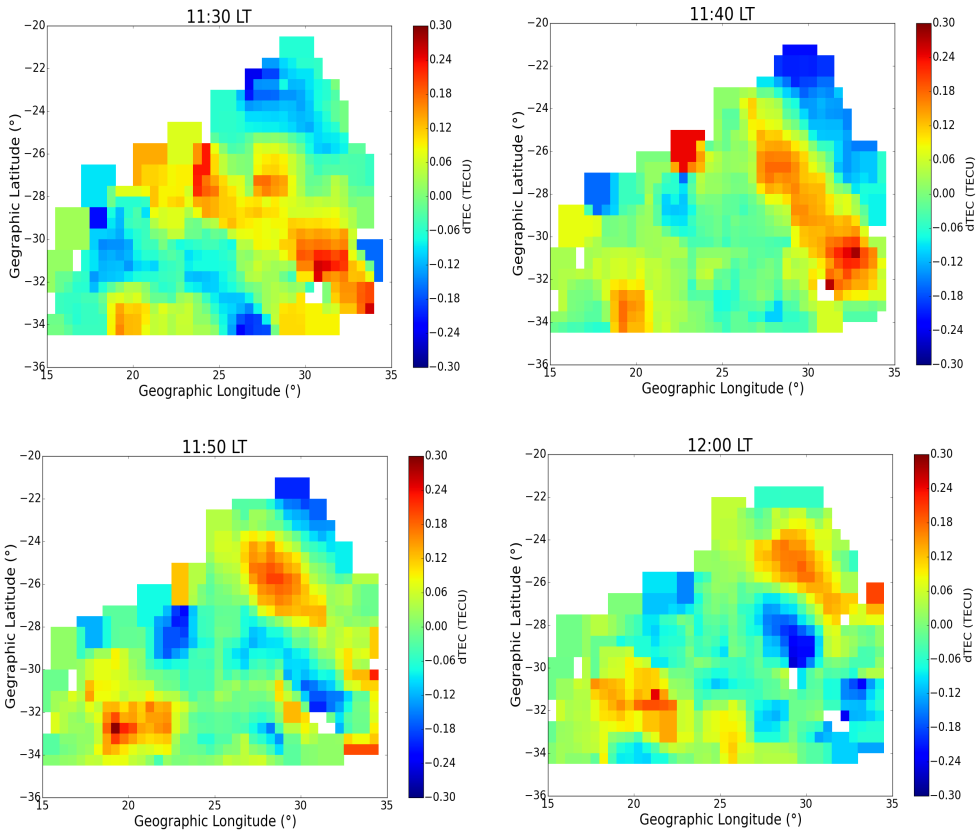

Figure 4.5: Detrended VTEC maps created at 10 minutes interval on 2010-03-13, from which propagation of TID can be obtained.

where the scaling parameter (s) represents the frequency, t is time, and τ is the time which $\psi(t)$ is translated (Mallat, 1999). For a given time series $x(t)$, the CWT, denoted by $W(s, \tau)$, is given by

$$W(s, \tau) = \int_{-\infty}^{\infty} x(t) \frac{1}{\sqrt{s}} \psi^* \Big(\frac{t - \tau}{s} \Big), \tag{4.26}$$

where $\psi(t)^*$ is the complex conjugate of $\psi(t)$ (Mallat, 1999). If Equation 4.26 is applied for different values of s and τ, the results are coefficients that are mapped on a frequency-time space.

Mother wavelets such as Haar, Daubechies, Paul, Meyer and Morlet are commonly used to convolve with $x(t)$ in Equation 4.26 (Mallat, 1999). In this project, the Morlet mother wavelet was used to map time series into frequency-time space. This wavelet was chosen because its shape resembles that of TIDs (e.g. Figure 4.4B and Figure 4.6). Therefore, Equation 4.26 will be high at frequencies (scaling parameter) that are close or equal to those of TID. The Morlet wavelet is given by

$$\psi(t) = \pi^{-1/4} e^{i\omega_0 t} e^{-t^2/2}. \tag{4.27}$$

Equation 4.27 is a sinusoidal wave with frequency ω_0 modulated by a Gaussian function (Mallat, 1999). According to Farge (1992), ψ is admissible, i.e satisfies Equation 4.24 if $\omega_0 = 6$. Equation 4.26 was applied with s ranging from 9.25×10^{-5} Hz (3 hours period) to 0.001667 Hz (5 minutes period); this ensured that Equation 4.27 assumes all frequencies that TIDs may have (Crowley and Rodrigues, 2012). Moreover, τ was incremented by 30 seconds in order to obtain frequencies at each time in the series. Figure 4.7A and B show a time series and $|W(1/s, \tau)|$, respectively. The period of the TID at each time corresponds to the maximum of $|W(1/s, \tau)|$ at that particular time. The black line in Figure 4.7B connects all $|W(1/s, \tau)|$ maxima at 30 seconds interval. The periods that correspond to the maxima range from 1.35 to 1.45 h, as can be seen from Figure 4.7.

4.4.2 Introduction to Particle Image Velocimetry

Particle image velocimetry (PIV) is an image processing technique that is used to estimate instantaneous velocity of a flowing fluid. PIV is performed by cross-correlating corresponding sub-images (interrogation windows) of two images of a flowing fluid captured at successive times (Westerweel, 1993). The first use of PIV in fluid was in the early 20^{th} century by Ludwig Prandtl

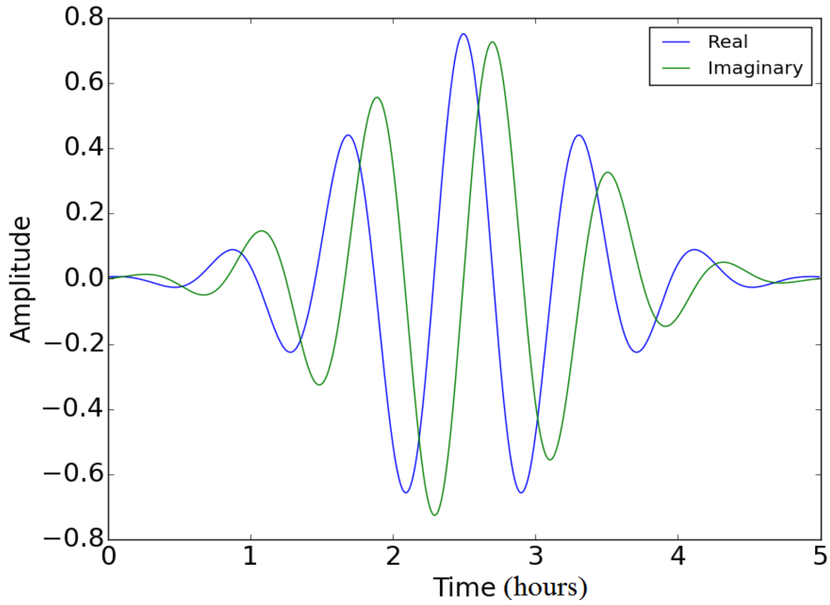

Figure 4.6: An example of Morlet wavelet.

(Raffel *et al.*, 2013). Presently, PIV is largely applied in aeronautical engineering (Raffel *et al.*, 2013), and in biological science where it is used to map the flow of aquatic biota (Stamhuis and Videler, 1995; Choi *et al.*, 2011).

The cross-correlation aims to find the displacement of the particles, which when divided by the time difference yields the velocity of the particles; and therefore, the velocity of the fluid (Westerweel, 1993). PIV is graphically illustrated in Figure 4.8. Frame 1 depicts a white flowing fluid seeded by black floating tracer particles. According to Westerweel (1993) the tracer particles are considered to be ideal, i.e:

- they flow in the same direction as the fluid,
- their displacement is the same,
- they do not change the properties of the fluid or its flow,

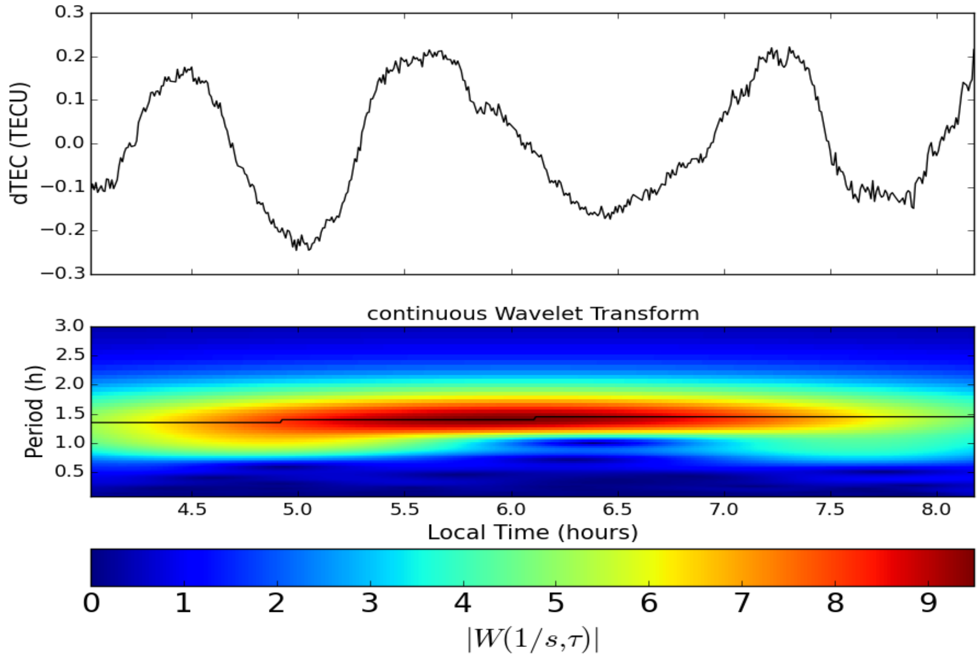

Figure 4.7: Time series of dTEC calculated for GPS satellite PRN24 at ANTH station on 2010-01-01 (top) and period-time wavelet decomposition of this calculated parameter (bottom).

- and they do not interact with each other.

This means that addition of new particles does not alter the motion of other particles. Consider the two corresponding interrogation windows marked in red in frames 1 and 2 of Figure 4.8. Initially (frame 1), the trace particles are positioned towards the left side of the interrogation window. Later (frame 2), they have moved to the right of the interrogation window. Cross-correlating the two windows results in a 2-dimensional correlation function that has a peak positioned where two interrogation windows match.

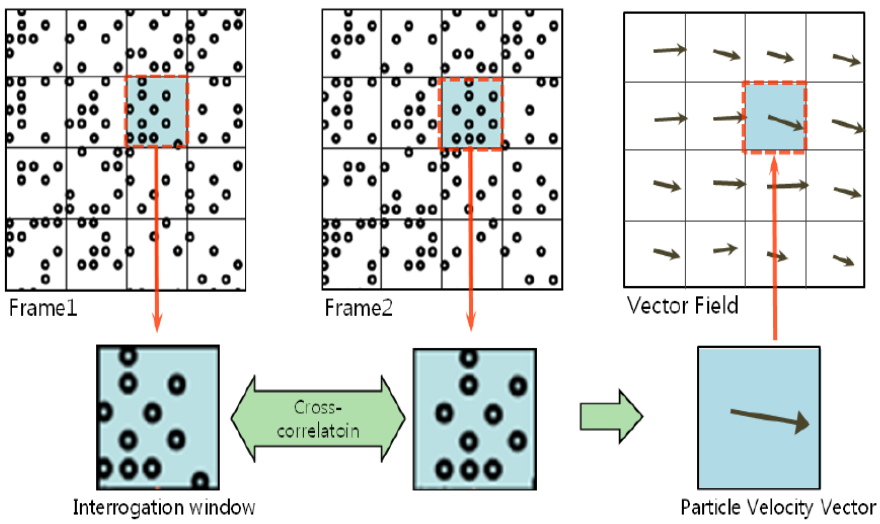

Figure 4.8: Graphical illustration of PIV (Choi *et al.*, 2011)

4.4.2.1 Cross Correlation

Suppose that frames 1 and 2 are represented by $G(l, m)$ and $H(l, m)$, where (l, m) are pixel coordinates. Cross correlation $\mathrm{C}(i, j)$ of the two frames is given by

$$\mathrm{C}(i, j) = \sum_{l=1}^{L} \sum_{m=1}^{M} G(l, m) H(l + i, m + j), \tag{4.28}$$

where L and M represent the number of rows and columns, respectively. Essentially, G is fixed and H moves over i units along the rows, and j units along the columns (Stearns and Hush, 2002). These units are referred to as shifts or lags, and are given by

$$\begin{aligned} i &= -\frac{L}{2}, -\frac{L}{2}+1, ..., 0, ..., \frac{L}{2}-1 \\ j &= -\frac{M}{2}, -\frac{M}{2}+1, ..., 0, ..., \frac{M}{2}-1. \end{aligned} \tag{4.29}$$

A zero lag occurs when the two frames coincide, i.e. when $(i, j) = (0, 0)$. If there was no particle motion between successive times, $\mathrm{C}(i, j)$ will have a peak at $(i, j) = (0, 0)$ (Choi *et al.*, 2011). However, if the particles did move, then the peak of $\mathrm{C}(i, j)$ will occur at (i, j), which corresponds to the displacement. The velocity of the particles can be obtained by dividing the displacement by the time difference between the two frames. The velocity can be plotted at the center of the interrogation window as shown in Figure 4.8 (particle velocity vector). This method can be repeated to cover the whole image size, until a vector field plot similar to that in Figure 4.8 is obtained.

The disadvantage of the correlation function given by Equation 4.28 is that the correlation coefficients do not have equal weight. This is because $\mathrm{C}(i, j)$ at lags closer to zero is computed using more data points at lags much greater than zero. In order to overcome this disadvantage, the normalized Pearson correlation, given by Equation 4.30, is used (Press, 2007):

$$C(i,j) = \frac{\sum_{l=1}^{L}\sum_{m=1}^{M}(G(l,m)-P_G)(H(l+i,m+j)-P_H)}{\sum_{l=1}^{L}\sum_{m=1}^{M}(G(l,m)-P_G)\sum_{l=1}^{L}\sum_{m=1}^{M}(H(l+i,m+j),-P_H)} \tag{4.30}$$

where

$$P_G = \frac{1}{LM}\sum_{l=1}^{L}\sum_{m=1}^{M} G(l,m), \tag{4.31}$$

and

$$P_H = \frac{1}{LM} \sum_{l=1}^{L} \sum_{m=1}^{M} H(l+i, m+j). \tag{4.32}$$

The displacements of particles are multiples of the image pixels. In order to estimate fractional (sub-pixel) displacement, correlation function should be interpolated, such that its peak is estimated to the desired resolution (Westerweel, 1993; Dabiri, 2006). Sub-pixel accuracy in this project was obtained by an interpolation scheme discussed in Section 4.4.3.

4.4.2.2 Uncertainties

According to Dabiri (2006) uncertainties in PIV may result from:

- the size of an interrogation window,
- the number of tracer particles in a window,
- the size of particles,
- out-of-plane motion,
- and time difference between two images.

If an interrogation window is small, such that the particles in frame 1 are not captured in frame 2, the PIV may result in spurious vectors. A low particles density in an interrogation window may yield more spurious vectors, because a small number data points will be available for cross-correlation. Moreover, Dabiri (2006) stated that bigger particle diameter increases accuracy. However, the diameter should not be too big such that particles appear to stationary between successive interrogation windows. Out-of-plane motion occurs when particles travel perpendicular to the image. When particles undergo such motion they may be captured in frame 1, but not in frame 2.

Another parameter that affects PIV accuracy is the time difference between successive images. Small time difference yields small velocities because particles have not traveled a large enough distance. If the time difference is too large tracer particles might undergo out-of-plane motion during their travel. In this project, the criteria to minimize the uncertainties are discussed in Section 4.4.3. Moreover, an outlier detector can be applied to remove spurious vectors.

4.4.3 PIV applied on TIDs

This project also introduces the use of the PIV method in space physics for the first time. PIV was used to infer velocities of TIDs by comparing successive dTEC maps. The dTEC enhancements or depletion on the maps were considered to be synonymous with tracer particles in PIV, and they move relative to the background dTEC. The following assumptions were made when applying PIV on dTEC maps:

- the motion of dTEC enhancements and depletion represent the motion of the observed TIDs,
- and pixels of dTEC enhancements and depletion mapped in the second interrogation window are the same ones that were mapped in the first window, as long as they are greater than the threshold; even though they may have less dTEC magnitude due to energy dissipation.

On the dTEC maps, an enhancement or depletion can be any value greater or less than zero TECU, respectively. Therefore, it was necessary to derive two threshold dTEC values, one for the enhancement, and the other for depletion. Positive/negative dTEC values which were greater/less or equal to the enhancement/depletion threshold were considered as dTEC disturbances.

The dTEC measurements from ANTH station for days 1 to 31 of 2010 were used to define the threshold for the year. This period was chosen because the 27 day Dst and Kp averages values (-6 and 1) indicating minimum magnetic activity were in January 2010. Maxima and minima dTEC values for all visible satellites were obtained at each 10^{th} minute for each day. These maxima and minima values were then averaged for the month and the averages set as thresholds for enhancements and depletions, respectively. To identify outliers for the whole month, dTEC values which did not satisfy

$$\mathrm{dTEC}_{median} - 3\ \mathrm{dTEC}_{amd} < \ \mathrm{dTEC}_i < \ \mathrm{dTEC}_{median} + 3\ \mathrm{dTEC}_{amd}, \quad (4.33)$$

were removed. In Equation 4.33, dTEC_i is the i^{th} $(i = 1, 2, ..., n)$ dTEC maximum/minimum, n is the total number of dTEC maxima/minima, dTEC_{median} and dTEC_{amd} are median, and absolute median deviation of the maximum/minima dTEC values. To find the median, the dTEC were arranged in an numerically ascending order, and the middle value was taken as the median (Taylor, 1997). The absolute median deviation was determined by

$$AMD = median(|\ \mathrm{dTEC}_i - median(\ \mathrm{dTEC})|), \quad (4.34)$$

as discussed by (Taylor, 1997). The thresholds used are 0.09 ± 0.04 TECU and -0.09 ± 0.04 TECU for enhancements and depletions, respectively.

Interrogation windows of dimensions 5°× 5° were used at 10 minutes intervals. These parameters were chosen to provide enough time, and space for TIDs to propagate within an interrogation window. For example, a MSTID that propagated at a velocity of 299 m/s would move a distance of 179.4 km in 10 minutes. This implies that the interrogation window size was sufficient for MSTIDs to be observed in successive windows. A LSTID with a velocity of 1000 m/s would propagate 600 km in 10 minutes. Therefore, the 5°× 5° window provided enough space so that the LSTID can propagate 600 km, if it traveled diagonally. However, if the LSTID propagates parallel to the breadth of the window, only velocities below 925 m/s would be determined. The size of the tracer particles (IPPs) were chosen to be fixed at 0.5°× 0.5°. Therefore the size of particles uncertainty was irrelevant. In the dTEC maps, out-of-plane motions were synonymous to TID dissipation. Since interrogation windows whose maximum/minimum dTEC were outside the thresholds were not correlated, this uncertainty could not be minimized.

Correlation using Equation 4.30 was performed only on interrogation windows which had at least one dTEC value that would be classified as disturbance according the thresholds. In Equation 4.30, $G(l,m)$ and $H(l,m)$ represented interrogation windows at a given time and 10 minutes later, respectively. The pixel coordinates l and m denoted the longitude and latitude coordinates on the dTEC maps, respectively. $H(l+i, m+j)$ represented the shifting of $H(l,m)$ by i and j pixels along the longitude and latitude, respectively. As discussed in Section 4.4.2.1, the shifts i and j correspond to displacement of the observed structure over the time difference between successive dTEC maps. In this project, positive and negative i were considered as eastward and westward displacements, respectively. The northward, and southward displacements corresponded to positive, and negative j, respectively. Similar to Section 4.4.2.1, the maximum displacement of a structure occurred at the peak of $C(i,j)$.

In order to obtain sub-pixel accuracy, the correlation function was interpolated to $0.1° \times 0.1°$ resolution using cubic interpolation. The displacements were multiplied by 0.1°, since each lag represents a displacement of 0.1°. Furthermore, the displacements were also multiplied by 111000 m in order to convert them from degrees to meters. This conversion was derived from the spherical model of the Earth (Duffett-Smith and Zwart, 2011), where the arc distance (d_{arc}) from the Earth's center over 1° is given by

$$d_{arc} = 2\pi \mathrm{R}_E \frac{\sigma}{360} \approx 111000 \text{ m}. \tag{4.35}$$

In Equation 4.35, $\sigma = 1°$ is the angle, and R_E is the Earth's radius given in Section 4.3.

The azimuth of propagation was calculated as the angle (in clockwise) between the latitude and the displacement vector. The latitude and longitude components of the velocity were obtained by dividing the displacements by the time difference between subsequent images. The interrogation was shifted by 0.5° until all portions of maps with data were fully covered. Figure 4.9A illustrates the velocity vector field plot for the TIDs depicted in Figure 4.5. A velocity vector was considered an outlier if its magnitude (v_i) or azimuth (θ) satisfied the conditions

$$v_{median} - 3v_{amd} > v_i > v_{median} + 3v_{amd} \qquad i = 0, ..., N \tag{4.36}$$

or

$$\theta_{median} - 3\theta_{amd} > \theta_i > \theta_{median} + 3\theta_{amd} \qquad i = 0, ..., N, \tag{4.37}$$

respectively. In Equation 4.36 and 4.37, N is the number of vectors, v_{median} and θ_{median} are the medians of the velocities and azimuths, respectively; v_{amd} and θ_{amd} denote the absolute median deviations of the respective quantities. The velocities, and azimuths were then averaged in order to obtain a mean velocity, and azimuth of the TIDs. The standard deviations were computed as errors associated with the method. As a result, the velocity (V_{PIV}), and the azimuth of the TID were given by

$$V_{PIV} = V_{median} \pm V_{amd}, \tag{4.38}$$

$$\Theta_{PIV} = \Theta_{median} \pm \Theta_{amd}, \tag{4.39}$$

respectively. V_{median} is the mean velocity, and V_{amd} the standard deviation. Similarly, Θ_{median}, and Θ_{amd} represent the mean, and absolute median deviation of the azimuth. After this outlier filter was applied to the velocities plotted in Figure 4.9A, the results were plotted in Figure 4.9B. The velocity, azimuth, and period of this TIDs were found to be 220.53 ± 84.83 m/s, 357.22 ± 12.53 °, and 0.9 ± 0.15 h, respectively. This TID was classified as a MSTID, according to Hernández-Pajares *et al.* (2012).

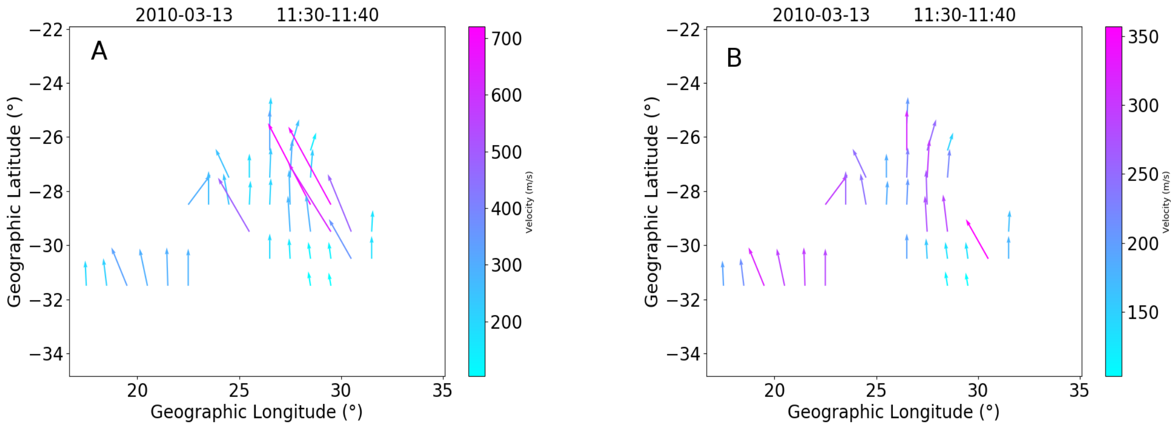

Figure 4.9: Bad velocity vector field plot for a MSTID that was observed on 2010-03-13 at 11:30 LT (A). The velocity vector field after removing outliers (B).

Chapter 5

Results and Discussion

5.1 Validation of the PIV method

The PIV method was applied to the detrended TEC (dTEC) maps created at 10 minutes intervals in each day of the year 2010. TIDs observed to propagate in a nearly northward direction were randomly selected and used to check the applicability of PIV on TIDs. These events occurred on 2010-06-09, 2010-06-12, 2010-07-10, and 2010-07-17. dTEC maps for these days were created on the latitude and time axis, as shown in Figure 5.1A, B, C, and D. The TIDs can be seen as dTEC enhancements propagating equatorward. Maxima of dTEC were selected at intervals of 0.5° latitude; these are marked by the black points in Figure 5.1. These points estimate the positions of the TIDs at a given time. This means that the motion of the TIDs was one dimensional, and the velocity could be estimated by the gradients of straight lines fitted on the black points. Therefore, straight lines were fitted on the maxima; their gradients were taken as estimates of velocities of the TIDs. The differences between the latitude of the selected maxima and the corresponding latitudes from the fitted lines were considered as the error of fitting.

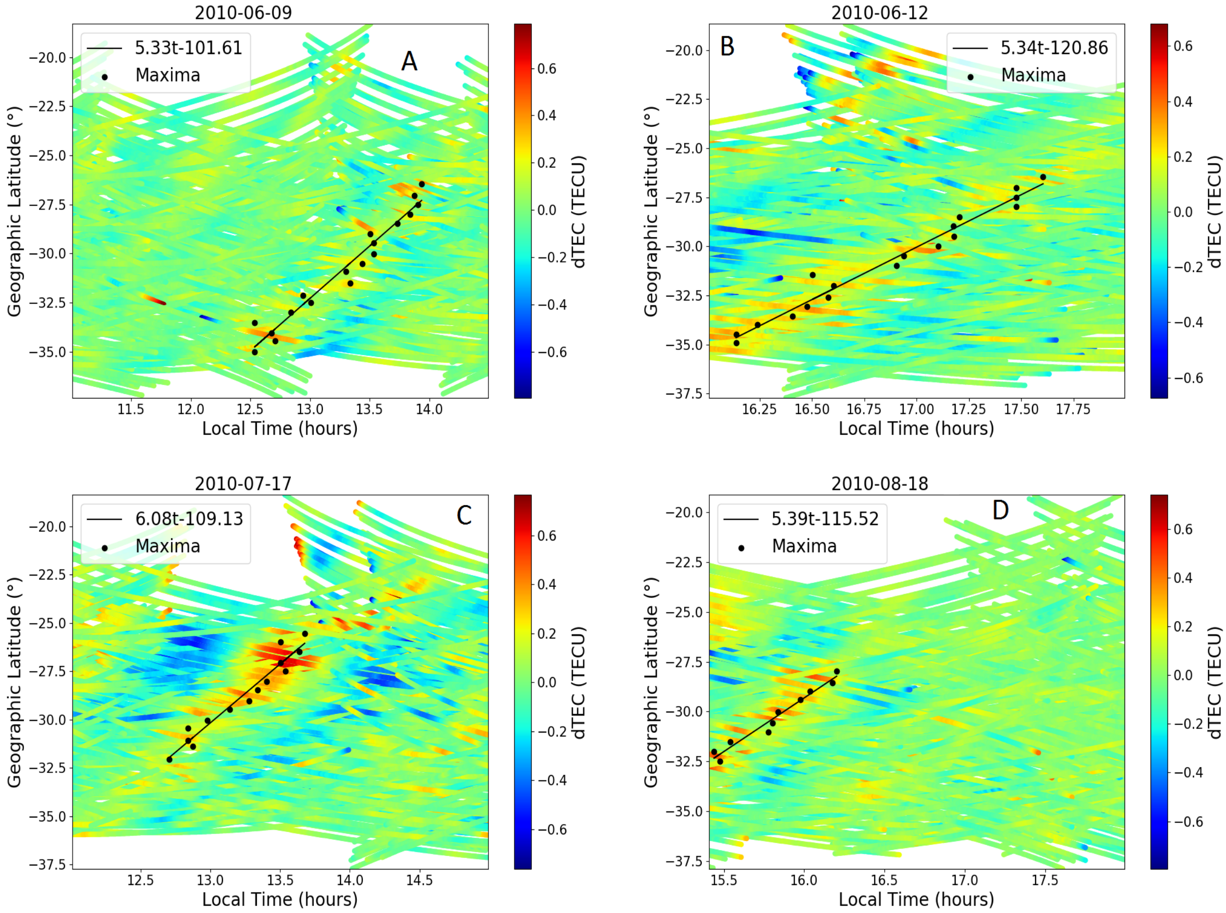

Figure 5.1: Northward TIDs that were observed on 2010-06-09 (A), 2010-06-12 (B), 2010-07-17 (C) and 2010-08-18 (D).

The error of the gradient (velocity) was computed by dividing the error of fitting by the time difference between the first and last dTEC maximum.

Table 5.1 lists the velocities and azimuths of the TIDs (denoted V_{piv} and Θ_{piv}, respectively) obtained by applying the PIV method, and fitting the straight lines shown in Figure 5.1A, B, C, and D. The gradients in Figure 5.1 were multiplied by 111000 m and divided by 3600 s in order to obtain the velocities (denoted by V_{line}) in Table 5.1. The velocity vectors of TIDs depicted in Figure 5.1A, B, C, and D are shown in Figure 5.2A, B, C, D, respectively. The velocities estimated by the gradients of the fitted lines are within the

Table 5.1: The TID velocities determined by the PIV method, and by gradients of the lines fitted in Figure 5.1A, B, C, and D.

Date of event	V_{piv} (m/s)	V_{line} (m/s)	Θ_{piv} (°)
2010-06-09	164.74 ± 31.50	164.34 ± 12.11	0 ± 2.45
2010-06-12	158.73 ± 39.61	164.65 ± 9.38	0.13 ± 5.67
2010-07-17	174.16 ± 53.59	187.47 ± 15.14	358.75 ± 9.10
2010-08-18	199.88 ± 35.67	166.19 ± 11.74	358.85 ± 5.13

velocity ranges obtained through the PIV method, suggesting that the PIV method can be reliably used to estimate velocities of TIDs.

5.2 Results

The PIV method detected 769 TIDs propagating over South Africa in 2010; 585 and 184 TIDs were observed during magnetically quiet and disturbed days, respectively. Magnetic disturbed dates were those in which the minimum Dst index was less than -30 nT (see Table 2.1), and the maximum Kp index was greater than 3 (MacDougall and Jayachandran, 2011). In this chapter, a MSTID will be a TID whose velocity, and period ranges include values less than 300 m/s, and 1 h, respectively (Munro, 1950; Chum *et al.*, 2012; Hernández-Pajares *et al.*, 2012). In contrast, a TID which has velocity, and period ranges greater or equal to 300 m/s, and 0.5 h, respectively, will be considered as a LSTID (Vadas and Lui, 2009; Ngwira *et al.*, 2012; Habarulema *et al.*, 2015). The periods were determined using the Morlet

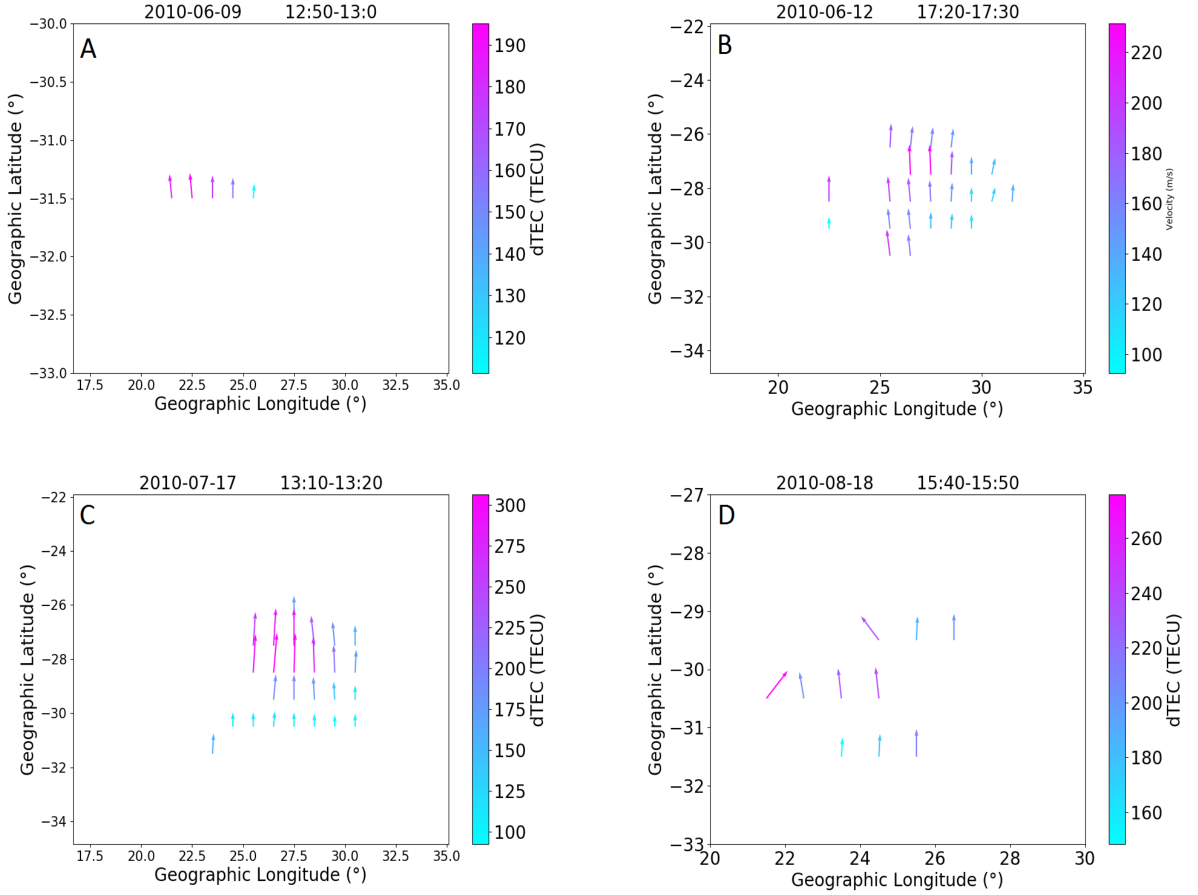

Figure 5.2: Velocity vector field plots for TIDs that were observed on 2010-06-09 (A), 2010-06-12 (B), 2010-07-17 (C) and 2010-08-18 (D).

function in wavelet analysis, as discussed in Section 4.4.1.

Section 2.3 discussed the variations that are experienced by the ionosphere, i.e. the diurnal, and seasonal. In Section 3.4, it was discussed that the passing of the solar terminator and magnetic storms induce TIDs. Therefore, in this project, the observed TIDs for the year 2010 were grouped into four categories: those that occurred during daytime, nighttime, passing of the solar terminator (i.e. twilight), and magnetic storms.

Daytime was considered as the time interval from 2 hours after sunrise until 2 hours before sunset. The sunrise and sunset data for 2010 were obtained from http://www.saao.ac.za/public-2/viewing-the-sky/sun/sun-rise-and-set-times-for-places-in-south-africa/. The time interval from 2 hours after sunset to 2 hours before sunrise was considered as nighttime. The twilight was defined as the time interval between 2 hours before and after sunrise/sunset. In order to study the seasonal behavior of the TIDs, the year was split into four southern hemisphere seasons: summer (day 1 to 60, and day 335 to 365), autumn (day 60 to 151), winter (day 152 to 243), and spring (day 244 to 334). These dates were obtained from http://www.weathersa.co.za/learning/weather-questions/82-how-are-the-dates-of-the-four-seasons-worked-out.

5.2.1 Daytime TIDs

The scatter plots in Figure 5.3 show that the majority of the MSTIDs propagated in the northerly direction, while the LSTIDs are scattered. In order to find seasonal trends, medians of the propagation parameters of these TIDs were computed. Table 5.2 summaries the average propagation parameters, where V_{PIV}, Θ_{PIV}, and T_m represent the medians of the velocity, direction, and period, respectively; the error ranges were obtained by computing the median absolute deviation of the respective parameters. As can be seen from Table 5.2, MSTIDs occur throughout the year. Munro (1950) made similar observations about daytime MSTIDs on the study performed in Australia. Table 5.2 suggests that the highest occurrence of the daytime MSTIDs during quiet conditions was in winter. This is in agreement with results stated by

Hernández-Pajares *et al.* (2012) on MSTIDs observed in New Zealand during solar minimum. Also, Park *et al.* (2014) obtained similar findings in the southern midlatitudes when they conducted a global climatology on gravity waves in the F region; using CHAMP observations.

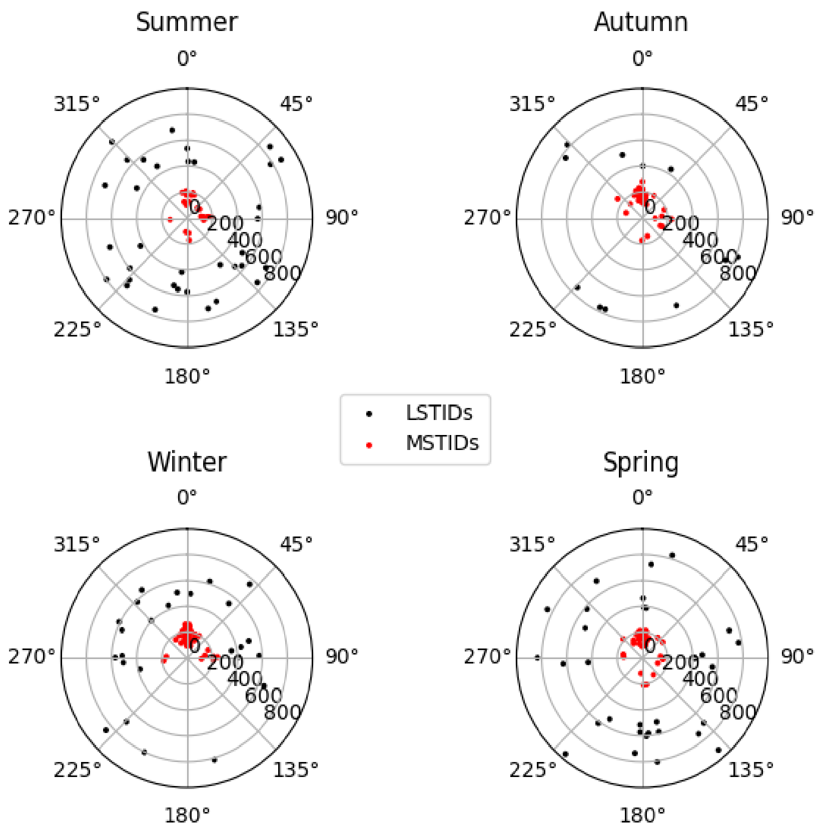

Figure 5.3: Occurrence of daytime TIDs in all seasons. The radii represent velocities (in m/s). The circumference represents the direction of propagation, where 0° corresponds to northward direction.

Figure 5.4 shows the number of observed daytime MSTIDs in 1 hour intervals, where the highest occurrence is between 15:00-16:00 in winter. This time range is within the one stated by Hernández-Pajares *et al.* (2012), where the maximum occurrence was between 12:00 and 16:00 LT. Munro (1958) also found that the number of daytime MSTIDs peaks around 12:00 LT in winter. It can be seen that in summer, autumn, and spring the maximum occurrence of daytime MSTIDs was around 12:00 LT.This suggests that number of MSTIDs is dependent on the solar zenith, because more MSTIDs are observed as the zenith angle decreases.

The seasonal variations in the velocities, and periods of the MSTIDs, and LSTIDs were not clear since these parameters intersect each other, as can be seen from error ranges in Table 5.2. Considering the error ranges in Table 5.2,

Table 5.2: A summary of propagation parameters of daytime TIDs that were observed in 2010.

Season	TID type	Events	V_{PIV} (m/s)	Θ_{PIV} (°)	T$_m$ (h)
Summer	MSTID	22	143.74 ± 29.37	32.99 ± 47.78	0.98 ± 0.11
	LSTID	34	588.80 ± 113.79	355.17 ± 118.60	1.12 ± 0.14
Autumn	MSTID	37	173.00 ± 24.20	0.00 ± 8.99	0.97 ± 0.11
	LSTID	11	746.87 ± 21.21	341.87 ± 117.96	1.12 ± 0.09
Winter	MSTID	76	185.68 ± 27.69	1.23 ± 4.89	1.06 ± 0.07
	LSTID	25	560.25 ± 78.35	339.99 ± 69.53	1.23 ± 0.19
Spring	MSTID	42	162.74 ± 24.10	359.79 ± 9.39	1.00 ± 0.09
	LSTID	31	603.58 ± 122.63	4.35 ± 98.35	1.09 ± 0.12

daytime MSTIDs propagated at velocities ranging from approximately 114 to 213 m/s during quiet geomagnetic conditions. Munro (1950) observed daytime MSTIDs that propagate at velocities up to 166 m/s. Chum *et al.* (2012), on a year long study from June 2010 using the HF Doppler sounding method, found that the velocity ranges for daytime MSTID in South Africa were from about 125 to 250 m/s. Hernández-Pajares *et al.* (2012) also obtained velocities (100-300 m/s) which include the ranges obtained in this study. This suggests consistency in the results presented in this study with those from previous studies in the southern midlatitudes.

It is clear from Table 5.2 that daytime MSTIDs propagated northwards (i.e. equatorward) in all seasons. These findings corroborate observations made by Morton and Essex (1978) on daytime MSTIDs in the southern midlatitudes. Chum *et al.* (2012), and Tyalimpi (2014) also obtained similar results for winter daytime MSTIDs in South Africa. Numerous authors have stated that MSTIDs are not easy to predict since they occur randomly (e.g. Beer, 1974; Hajkowicz, 1990; Hocke and Schlegel, 1996). In this thesis and other related work (Munro, 1950, 1958; Chum *et al.*, 2012; Hernández-Pajares *et al.*, 2012), daytime MSTIDs were found to propagate in the equatorward direction. This means that daytime MSTIDs are manifestations of daily occurring AGWs. According to MacDougall and Jayachandran (2011), there are AGWs that originate in the lower atmosphere as result of direct heating by the Sun. Another source of AGWs is the wind turbulence on the lee side of South Africa mountain ranges (De Villiers and Van Heerden, 2001; Van Der Mescht, 2012). These AGWs could have instigated the daytime MSTIDs.

Although for a long time LSTIDs have been associated mainly with magnetic storms (e.g. Thome, 1960, 1968; Chimonas, 1970a; Hernandez and Roble, 1978; Hocke and Schlegel, 1996), the occurrence of LSTIDs during magnetically quite conditions has been discussed by in the past (e.g. Vadas and Lui, 2009; Ding *et al.*, 2014). Table 5.2 suggests that the LSTIDs propagated with

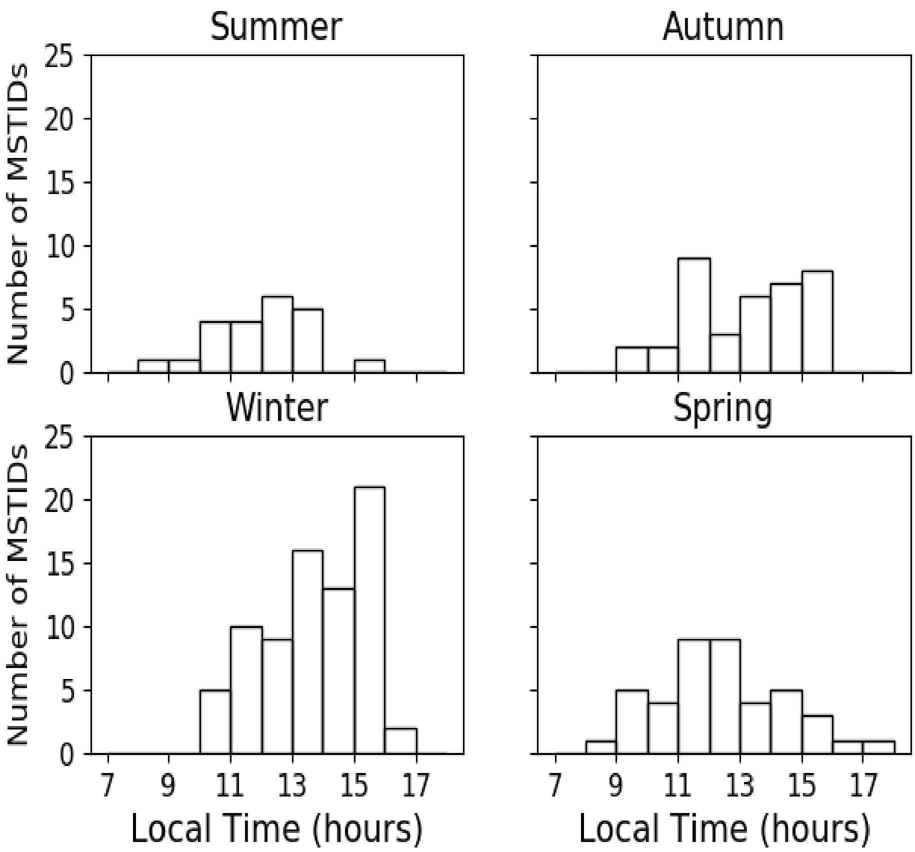

Figure 5.4: Time of occurrence of daytime MSTIDs for different seasons

velocities from approximately 455 to 767 m/s. These velocities are comparable with those of LSTIDs in South Africa during magnetic storms (Ngwira *et al.*, 2012; Katamzi and Habarulema, 2014). Furthermore, Table 5.2 suggests that daytime LSTIDs propagated equatorward in all seasons. These equatorward daytime LSTIDs were also observed in a climatological study of LSTIDs in China and North America from 2011 to 2012 (Ding *et al.*, 2014).

Figure 5.5 suggests that in summer the peak LSTID observation is between 12:00 and 13:00 LT. There was a small number of LSTIDs in autumn, and hence the maximum occurrence is not clearly defined. The LSTIDs might have been induced by secondary AGWs that may have originated when AGWs from the lower atmosphere dissipate in the thermosphere. These AGW were observed by Vadas and Lui (2009), in their study in Brazil. Park *et al.* (2014) also confirmed such secondary AGWs in their global study.

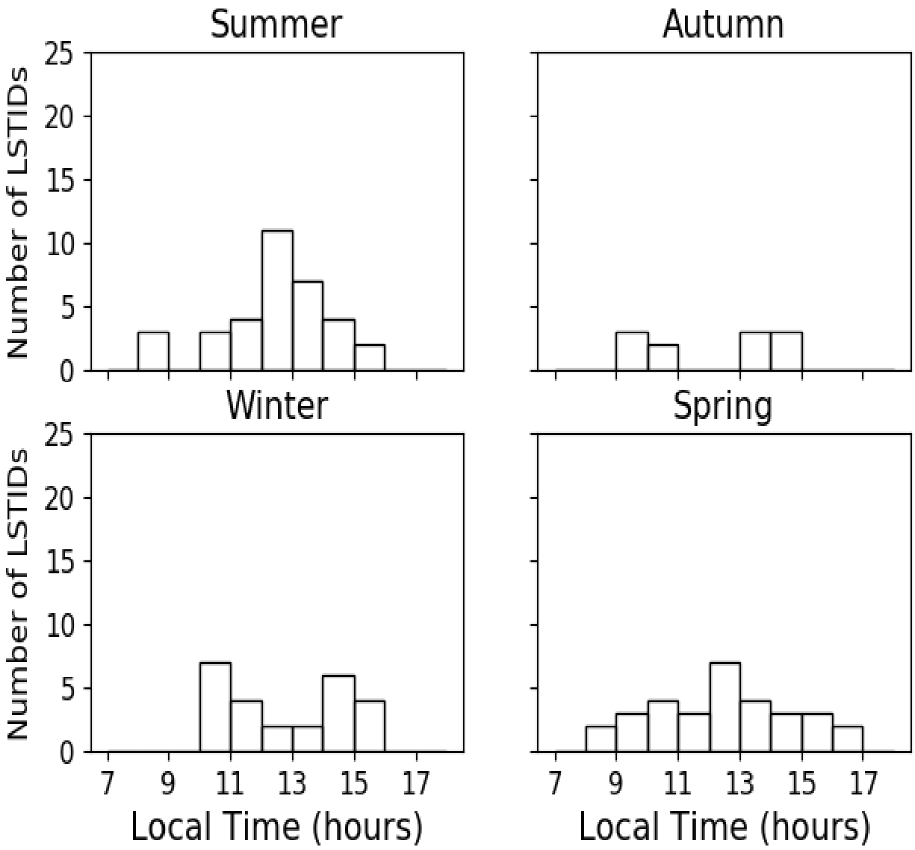

Figure 5.5: Time of occurrence of daytime LSTIDs for different seasons

5.2.2 Passing of Solar Terminator

The TIDs which occurred during the passing of the solar terminator are plotted in Figure 5.6. They are 254 in total, where 78% were LSTIDs, and 22%

were MSTIDs. Most TIDs (76%) were observed during the passing of the morning solar terminator. The propagation parameters for these TIDs are summarized in Table 5.3.

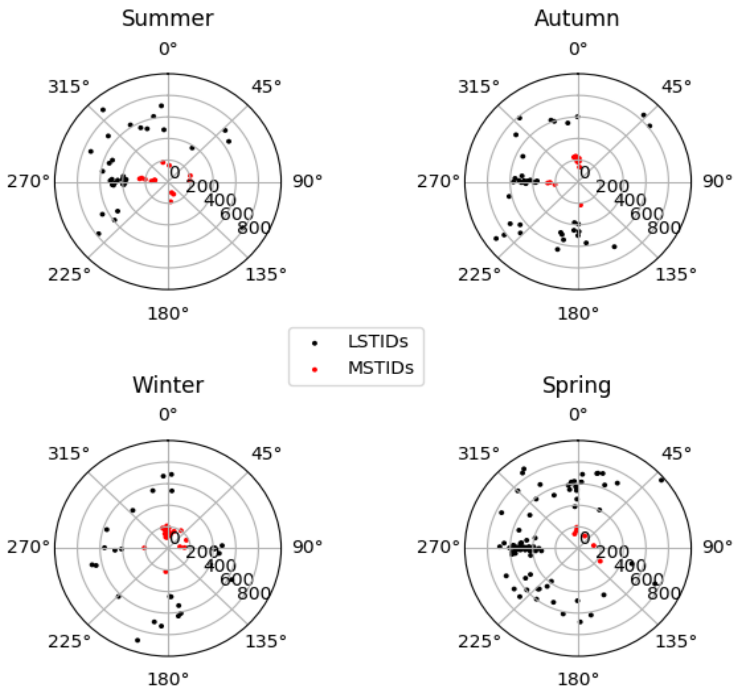

Figure 5.6: TIDs which occurred during the passing of the morning solar terminators

The results suggest that the MSTIDs propagated equatorward in all seasons. Similar observations of were made by Chum *et al.* (2012). Moreover, it can be seen from Figure 5.6 that there are a number of MSTIDs which propagated westward. These results agree with Hernández-Pajares *et al.* (2012); they found equatorward, and westward propagation directions for MSTIDs in New Zealand between 04:00 and 08:00 LT. Due to the intersection of the velocity ranges, seasonal variations cannot be made without ambiguity.

Table 5.3: Propagation parameters of TIDs that were observed during the passing of the morning terminator.

Season	TID type	Events	V_{PIV} (m/s)	Θ_{PIV} (°)	T_m (h)
Summer	MSTID	13	183.40 ± 37.64	346.14 ± 70.15	1.03 ± 0.06
	LSTID	35	521.5 ± 121.80	274.20 ± 17.88	1.09 ± 0.11
Autumn	MSTID	12	212.13 ± 22.45	358.66 ± 5.93	1.06 ± 0.08
	LSTID	43	522.73 ± 78.54	270.00 ± 37.16	1.22 ± 0.19
Winter	MSTID	24	154.63 ± 28.87	356.12 ± 7.76	1.02 ± 0.08
	LSTID	25	560.24 ± 94.01	356.52 ± 99.31	1.31 ± 0.12
Spring	MSTID	6	151.89 ± 18.63	12.20 ± 21.08	1.05 ± 0.08
	LSTID	95	536.32 ± 80.09	271.25 ± 23.15	1.33 ± 0.12

The LSTIDs propagated northward in winter, westward in summer, autumn, and spring, as can be seen from Table 5.3. The westward propagating LSTIDs during the passing of the solar terminator have been reported by MacDougall and Jayachandran (2011) in the northern midlatitudes, and by Afraimovich *et al.* (2009) in California and Japan. Although these studies were not performed in the south midlatitudes, their findings are comparable with the results in this thesis, because the solar terminator travels from east to west globally.

Considering that the solar terminator propagates westward, the westward propagating TIDs may have been induced by AGWs that were excited by the terminator. A similar suggestion was made by Hernández-Pajares *et al.* (2012) and Ding *et al.* (2014). However, this does not imply that the TIDs which were not directed westward were not induced by the solar terminator; they could be influenced by AGW that originate from solar heating (MacDougall and Jayachandran, 2011). Most of twilight TIDs (76%) occurred during the passage of the morning solar terminator; implying that the morning terminator was more effective in instigating TIDs compared to the afternoon terminator. These findings are consistent with those obtained by MacDougall and Jayachandran (2011) and Chum *et al.* (2012).

5.2.3 Nighttime TIDs

Figure 5.7 shows the seasonal distribution of nighttime MSTIDs and LSTIDs with respect to the preferred propagation velocity and direction during nighttime in 2010. There were 50 observed TIDs for the whole year, where 13 of them were MSTIDs, and 37 were LSTIDs. It is clear that there were much less TIDs observed during nighttime compared to other time periods. The reason why such few observations were made could lie in wavelengths of the nighttime MSTIDs. It could be that the MSTIDs were too localized. As a result, they could not appear on the TEC maps which had $0.5° \times 0.5°$ resolution. In addition, these MSTIDs could have been attenuated at lower altitudes before they could cause large-scale AGWs discussed in Section 3.7.2; hence the few observed LSTIDs. These TIDs are statistically insignificant for analysis, and cannot lead to conclusive discussions. The northward and southward propagating the nighttime MSTIDs seem to be consistent with observations made by Ogawa *et al.* (2009) in the northern midlatitudes during magnetically quite conditions ($0 \leq K_p \leq 1$). Ogawa *et al.* (2009) stated that the MSTIDs originated from high latitudes. Furthermore, night MSTIDs are able to propagate distances of about 4000 km. Similar observations on nighttime MSTIDs were also made by Kelley (2011) in the northern midlatitudes. The LSTIDs depicted in Figure 5.7 might have been caused by secondary

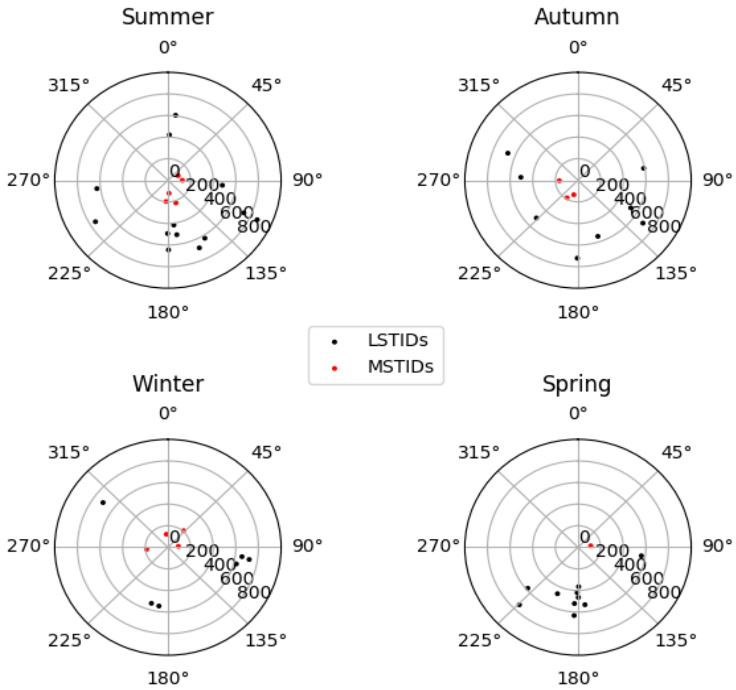

Figure 5.7: Occurrence of nighttime TIDs. The radii represent velocity (in m/s), and the circumference represents the direction of propagation.

AGWs that originate when an AGW from the lower atmosphere breaks in the thermosphere (Vadas and Lui, 2009).

5.2.4 During geomagnetically disturbed conditions

The geomagnetic activity for the year 2010 was monitored using Dst and Kp index obtained from https://omniweb.gsfc.nasa.gov/form/dx1.html. Hourly Dst, and Kp indices for the 2010 are plotted in Figure 5.8A and B, respectively. As stated earlier in this chapter, the period with Kp $>$ 3 and Dst $\leq$ -30 nT was considered a magnetic storm, where a weak storm is classified as -30 nT $\leq$ Dst $>$ -50 nT and a moderate storm as -50 nT $\leq$ Dst $>$ -100 nT according to Tsurutani *et al.* (1997). Figure 5.8C shows a histogram (1 day bins) of TIDs that were observed during magnetic storms. In total, there were

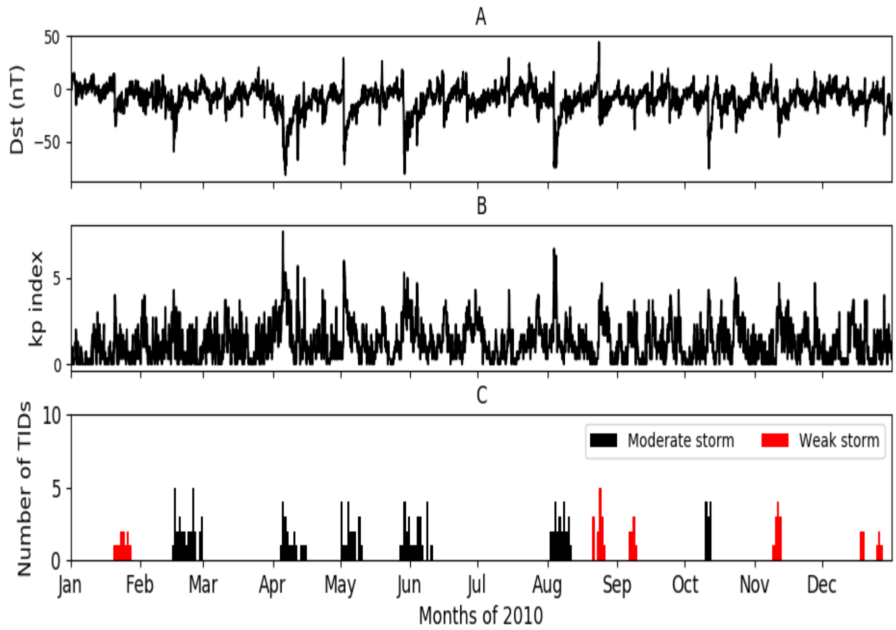

Figure 5.8: Geomagnetic activity for 2010. The daily minima Dst (A), and maxima Kp (B). Occurrence of TIDs during weak (red) and moderate (black) storms (C).

184 TIDs that were observed during geomagnetically disturbed conditions; 52 occurred during weak, and 132 were observed during moderate storms. Moreover, Table 5.4 suggests that the number of MSTIDs, and LSTIDs increased with geomagnetic activity. Ding *et al.* (2014) obtained similar results in China for a study performed between years 2011 and 2012. Furthermore, Table 5.4 suggests that MSTIDs propagated northwards during disturbed conditions. This observation supports Tyalimpi (2014), who reported a night-time MSTID propagating northwestward during the weak storm of January 2010 (see Figure 5.8). Furthermore, Sindelarova *et al.* (2012) reported north-

ward propagating MSTIDs in the southwestern region of South Africa during moderate magnetic storms. In northern hemisphere midlatitudes, a south-westward (equatorward) propagating daytime MSTID was observed during a great storm (Dst $\leq$ -350) (Nishioka *et al.*, 2009). According to Nishioka *et al.* (2009), the MSTID propagated in the same direction as those observed during quite conditions. A similar behavior can be seen from the current results shown in Table 5.2 and Table 5.4. The LSTIDs preferred westward

Table 5.4: Propagation parameters of TIDs that were observed during weak, and moderate magnetic conditions.

Storm	TID type	No. TIDs	V_{PIV} (m/s)	Θ_{PIV} (°)	T_m (h)
Weak	MSTIDs	18	167.66 ± 33.61	359.91 ± 52.08	0.98 ± 0.11
	LSTIDs	34	588.92 ± 79.37	312.83 ± 72.04	1.19 ± 0.19
Moderate	MSTIDs	48	164.66 ± 34.56	359.56 ± 9.29	1.04 ± 0.11
	LSTIDs	84	560.66 ± 103.59	283.48 ± 69.4	1.17 ± 0.13

direction of propagation as can be seen in Table 5.4. Their velocities, and directions are comparable with those obtained in previous studies in South Africa. Ngwira *et al.* (2012) observed a LSTID propagating northward with a velocity of 438 m/s during great magnetic storm on 2005-05-15. Also, Katamzi and Habarulema (2014) reported a LSTID propagating northward at a velocity of approximately 492 m/s.

The TIDs observed during magnetically disturbed periods could have been induced by AGWs that originate from the auroral region during magnetic storms. As discussed in Section 3.4, highly energetic particles are injected into the Earth at high latitudes. These particles then penetrate into the neutral atmosphere, which they heat up through collision. As a results, the neutral atmosphere expands and bulges, thereby converting thermal energy into gravitational potential energy. Equatorward AGWs will be generated when the Earth's gravity restore equilibrium in the atmosphere (Thome, 1960, 1968; Hernandez and Roble, 1978). However, the solar terminator, and AGW generated from the lower atmosphere may have had a contribution in some of the TIDs.

Chapter 6

Summary and Conclusions

This thesis presented a statistical analysis of TIDs that were observed in 2010, where the PIV method was applied for the first time in space physics. The TEC data were obtained from Trignet GPS receivers located in South Africa (ftp://ftp.trignet.co.za/). The periods of the TIDs were determined using the Morlet function in wavelet analysis. The results were then used to perform statistical analysis.

6.1 Conclusions

The aims of this project, as discussed in Section 1.2 were to: (1) determine propagation parameters of TIDs using GPS derived TEC data, (2) and perform a statistical analysis on TIDs in South Africa using TEC data acquired in 2010. The conclusions from this study are as follows:

- **Daytime**

  MSTIDs propagated northward (i.e. equatorward) in all seasons. Their maximum occurrence was in winter, around 15:00 and 16:00 LT. This agrees with previous studies performed in the midlatitudes (e.g. Munro, 1958; Hernández-Pajares *et al.*, 2012). The minimum occurrence of daytime MSTIDs was in summer. MSTIDs propagated at velocities from about 114 to 213 m/s. LSTIDs showed similar propagation directions as the MSTIDs. They propagated at velocities of approximately 455 to 767 m/s. Their occurrence was highest at 12:00-13:00 LT in summer.

- **Solar terminator**
  During the passage of the morning solar terminator, more LSTIDs (78%) were observed as opposed to MSTIDs. The LSTIDs propagated in westward directions in summer, autumn, and spring; they followed the same direction as the solar terminator. This kind of behavior of LSTIDs was also found by MacDougall and Jayachandran (2011); Ding *et al.* (2014). The afternoon solar terminator was found to be less effective in producing TIDs compared to the morning terminator, which agrees with the findings obtained by MacDougall and Jayachandran (2011); Chum *et al.* (2012).

- **Nighttime**
  Very few nighttime TIDs were observed. This could have been due to localized (short wavelengths), such that they could not be resolved on the TEC maps of $0.5^{\circ} \times 0.5^{\circ}$ resolution used in this study. The TIDs that were observed seemed to have been excited by gravity waves generated in the high latitude regions (Ogawa *et al.*, 2009; Kelley, 2011).

- **Magnetically disturbed conditions**
  The TIDs propagated equatorward. This means that they were induced by AGWs that originate from the auroral regions when the storms occurred (Thome, 1968; Hernandez and Roble, 1978; Chimonas, 1970a).

6.2 Recommendations for Future Work

The PIV method was applied with success in determining velocities of TIDs. However its accuracy, i.e. reduction in velocity, and azimuths error ranges, can be improved with an availability of a denser GPS receiver network, so that TEC maps can have more IPPs, which will lead to better mapping of TIDs. Moreover, longer data set may improve statistical findings on TIDs.

References

Afraimovich, E., Voeykov, S., Perevalova, N., and Ratovsky, K.: Large-scale traveling ionospheric disturbances of auroral origin according to the data of the GPS network and ionosondes, Advances in Space Research, 42, 2008.

Afraimovich, E., Edemskiy, I., Voeykov, S., Yasyukevich, Y. V., and Zhivetiev, I.: The first GPS-TEC imaging of the space structure of MS wave packets excited by the solar terminator, Annales Geophysicae, 27, 2009.

Afraimovich, L. E., Palamartchouk, K., and Perevalova, N. P.: GPS radio interferometry of travelling ionospheric disturbance, Journal of Atmospheric and Solar Terrestrial Physics, 60, 1998.

Afraimovich, E. F. and Edemskiy, I. K. and Leonovich, A. S. and Leonovich, L. A. and Voeykov, S. V: MHD nature of night-time MSTIDs excited by the solar terminator, Geophysical Research Letters, 36, 2009.

Anthes, R. A., Bernhardt, P. A., Chen, Y., Cucurull, L., Dymond, K. F., Ector, D., Healy, S. B., Ho, S. P., Hunt, D. C., Kuo, Y., Liu, H., Manning, K., Mccormick, C., Meehan, T. K., Randel, W. J., Rocken, C., Schreiner, W. S., Sokolovskiy, S. V., Syndergaard, S., Thompson, D. C., Trenberth,

K. E., Wee, T., Yen, N. L., and Zeng, Z.: THE COSMIC/FORMOSAT-3 Mission Early Results, American Meteorological Society, 89, 2008.

Artru, J., Ducic, V., Kanamori, H., Lognonn, P., and Murakami, M.: Ionospheric detection of gravity waves induced by tsunamis, Geophysical Journal International, 160, 2005.

Beer, T.: Atmospheric gravity waves, Adam Hilger LTD, 1974.

Bhonsle, R.: Diurnal Variations of Large-Scale Ionospheric Irregulaties, Journal of Geophysical Research, 19, 1966.

Bhonsle, R. V., da Rosa, V. A., and Garriott, O.: Measurements of the Total Electron Content and the Equivalent Slab Thichness of the Midlatitude Ionosphere, Radio Science, 69D, 1965.

Borovsky, J. E. and Denton, M. H.: Differences between CME-driven storms and CIR-driven storms, Journal of Geophysical Research, 111, 2006.

Buchert, S., F., Z., Sust, M., Andr, M., Eriksson, A., Wahlund, J. E., and Opgenoorth, H.: SWARMobservations of equatorial electrondensities and topside GPS track losses, Geophysical Research Letters, 42, 2015.

Chimonas, G.: The Equatorial Electrojet as a Source of Long Period Travelling Ionspheric Disturbances, Planetary and Space Science, 18, 1970a.

Chimonas, G.: Internal Gravity-Wave Motions Induces in the Earth's Atmosphere by Solar Eclipse, Journal of Geophysical Research, 75, 1970b.

Choi, S. M., Kim, W. H., Côté, D., Park, C.-W., and Lee, H.: Blood cell assisted in vivo Particle Image Velocimetry using the confocal laser scanning microscope, Optics express, 19, 2011.

Chum, J., Athieno, R., Baše, J., Burešová, D., Hruška, F., Laštovička, J., McKinnell, L., and Šindelářová, T.: Statistical investigation of horizontal propagation of gravity waves in the ionosphere over Europe and South Africa, Journal of Geophysical Research: Space Physics, 117, 2012.

Crowley, G. and Rodrigues, F. S.: Characteristics of traveling ionospheric disturbances observed by the TIDDBIT sounder, Radio Science, 47, 2012.

Dabiri, D.: Cross-correlation digital particle image velocimetrya review, Turbulencia. ABCM, Curitiba, 2006.

De Villiers, M. P. and Van Heerden, J.: Clear air turbulence over South Africa, Meteorological Applications, 8, 2001.

Desseler, A. J. and Parcker, E. N.: Hydromagnetic theory of geomagnetic storms, Journal of Geophysical Research, 64, 1959.

Dieminger, W., Hartman, G. K., and Reinhart, L.: The Upper Atmosphere: Data Analysis and Interpretation, Springer-Verlag, 1996.

Ding, F., Wan, W., Ning, B., Zhao, B., Li, Q., Wang, Y., Hu, L., Zhang, R., , and Xion, B.: Observations of poleward-propagating large-scale traveling discussions ionospheric disturbances in southern China, Annales of Geophysicae, 31, 2013.

Ding, F., Wan, W., Li, Q., Zhang, R., Song, Q., Ning, B., Liu, L., Zhao, B., and Xiong, B.: Comparative climatological study of large-scale traveling ionospheric disturbances over North America and China in 2011–2012, Journal of Geophysical Research: Space Physics, 119, 2014.

Dobson, D.: Exploring The Atmosphere, Oxford University Press, 2 edn., 1968.

Duffett-Smith, P. and Zwart, J.: Practical Astronomy with your calculator or spreadsheet, Cambridge University Press, 2011.

Edwards, A. L.: An introduction to linear regression and correlation., 1976.

Farge, M.: Wavelet transforms and their applications to turbulence, Annual review of fluid mechanics, 24, 1992.

Fees, W. and Stephens, S.: Evaluation of GPS ionospheric time delay algorithm for single frequency users, in: Proceedings, IEEE PLANS'86, IEEE Position, Location, and Navigation Symposium, 1986.

Ferguson, M.: GPS Land Navigation: A Complete Guidebook for Backcountry Users of the NAVISTAR Satellite System, Glassford Publishing, 1997.

Force, U. A.: Space Segment, URL `http://www.gps.gov/systems/gps/space/`, 2017.

Foster, J. C. and Rich, F. J.: Prompt midlatitude electric field effects during severe geomagnetic storms, Journal of Geophysical Research, 103, 1998.

Fritts, D. C. and Alexander, M. J.: Gravity wave dynamics and effects in the middle atmosphere, Reviews of geophysics, 41, 2003.

Gonzalez, W., Joselyn, J. A., Kamide, Y., and Kroehl, H. W.: What is a magnetic storm, Journal of Geophysical Reasearch, 99, 1994.

Goodman, J. M.: Space Weather & Telecommunications, Springer Science, 2005.

Gorney, D.: Solar Cycle Effect on the Near-Earth Space Environment, Geophysical Reviews, 28, 1990.

gps.gov: Space Segment, https://www.gps.gov/systems/gps/space/, [Online; accessed 2017-06-17], 2017a.

gps.gov: Control Segment, https://www.gps.gov/systems/gps/control/, [Online; accessed 2017-06-19], 2017b.

gps.gov: Space Segment, https://www.gps.gov/systems/gnss/, [Online; accessed 2018-9-25], 2017c.

Habarulema, J. B., McKinnell, L.-A., Burešová, D., Zhang, Y., Seemala, G., Ngwira, C., Chum, J., and Opperman, B.: A comparative study of TEC response for the African equatorial and mid-latitudes during storm conditions, Journal of Atmospheric and Solar-Terrestrial Physics, 102, 2013.

Habarulema, J. B., Katamzi, Z. T., and Yizengaw, E.: First observations of poleward large-scale traveling ionospheric disturbance over the African sector during geomagnetic storm conditions, Journal of Geophysical Research: Space Physics, 120, 2015.

Habarulema, J. B., Katamzi, Z. T., Yizengaw, E., Yamazaki, Y., and Seemala, G.: Simultaneous storm time equatorward and poleward large-scale TIDs on a global scale, Gephysical Research Letters, 43, 2016.

Hajkowicz, L. A.: A Global study of large scale travelling ionospheric disturbances (TIDs) following a step-like onset of auroral substorms in both hemispheres, Planetary and Space Science, 38, 1990.

Hargreaves, J. K.: The upper atmosphere and solar-terrestrial relations: an introduction to the aerospace environment, Van Nostrand Reinhold Co. Ltd., 1979.

Hargreaves, J. K.: The solar-terrestrial environment, Cambridge University Press, 1992.

Heisler, L. H. and Whitehead, J. D.: F-region traveling disturbances and sporadic-E ionization, Journal of Geophysical Research, 65, 1960.

Herman, J. R.: Spread F and ionospheric F-region irregularities, Reviews of Geophysics, 4, 1966.

Hernandez, G. and Roble, R. G.: Observations of large-scale thermospheric waves during geomagnetic storms, Journal of Geophysical Research, 83, 1978.

Hernández-Pajares, M., Juan, J., Sanz, J., and Aragón-Àngel, A.: Propagation of medium scale traveling ionospheric disturbances at different latitudes and solar cycle conditions, Radio Science, 47, 2012.

Hines, C. O.: Internal atmospheric gravity waves at ionospheric heights, Canadian Journal of Physics, 38, 1960.

Hines, C. O.: The upper atmopsphere in motion, Quarterly Journal of the Royal Meteorological Society, 89, 1963.

Hines, C. O.: Atmospheric gravity waves: a new toy for the wave theorist, Radio Science Journal of Research, 69D, 1965.

Hines, C. O.: Ionospheric irregularilaties produced by internal atmospheric gravity waves, Journal of Atmospheric and Terrestrial Physics, 36, 1974a.

Hines, C. O.: Propagation velocities and speeds in the ionospheric waves: A review, Journal of Atmospheric and Terrestrial Physics, 36, 1974b.

Hocke, K. and Schlegel, K.: A review of atmospheric gravity waves and travelling ionospheric disturbances: 1982-1995, Ann. Geophysicae, 14, 1996.

Hofmann-Wellenhof, B., Lichtenegger, H., and Collins, J.: GPS: theory and practice, Springer-Verlag Wien, 1992.

Hooke, W. H.: Ionospheric Irregularities Produced by Internal Atmospheric Gravity Waves, Journal of Atmospheric and Terrestrial Physics, 30, 1968.

Hooke, W. H.: The ionospheric response to internal gravity waves 1. The F2-region response, Journal of Geophysical Research: Space Physics, 70, 1970.

Jorgensen, P. S.: An assessment of ionospheric effects on the GPS user, Navigation, 36, 1989.

Kamide, Y. and Chain, A.: Handbook of the Solar-Terrestrial Environment, Springer, 2007.

Karpachev, A. T.: Detection of large scale TIDs associated with the dayside cusp using SuperDARN, Journal of Atmospheric and Solar-Terrestrial Physics, 72, doi:10.1016/j.jastp.2010.02.018, 2010.

Katamzi, Z. T. and Habarulema, J. B.: Traveling ionospheric disturbances observed at South African midlatitudes during the 29–31 October 2003 geomagnetically disturbed period, Advances in Space Science Research, 53, 2014.

Kelley, M. C.: On the origin of mesoscale TIDs at midlatitudes, Annales Geophysicae, 29, 2011.

Kelly, M. C.: The Earth's ionosphere: plasma physics and electrodynamics, Elsevier Inc., 2009.

Kintner, P. M., Coster, A. J., Fuller-Rowell, T., Mannucci, A. J., Mendillo, M., and Heelis, R.: Midlatitude ionospheric dynamics and disturbances, American Geophysical Union, 2008.

Klobuchar, J. A.: Design and characteristics of the GPS ionospheric time delay algorithm for single frequency users, in: PLANS'86-Position Location and Navigation Symposium, 1986.

Kohl, H., Ruster, R., and Schlegel, K.: Mordern Ionospheric Science, European Geophysical Society, 1996.

Lastovicka, J., Bourdillon, A., *et al.*: Ionospheric effects on terrestrial communications: Working Group 3 overview, Annals of Geophysics, 2004.

Leitinger, R. and Rieger, M.: The TID model for modulation of large scale electron density models, Annals of Geophysics, 48, 2005.

Lilensten, J.: Space Weather: Research Towards Application in Europe, Springer, 2007.

Loewe, C. and Prölss, G. W.: Classification and mean behavior of storms, Journal of Geophysical Research, 102, 1997.

MacDougall, J. and Jayachandran, P.: Solar terminator and auroral sources for traveling ionospheric disturbances in the midlatitude F-region, Journal of Atmospheric and Solar-Terrestrial Physics, 73, 2011.

MacLeaod, M.: Sporadic E.I. Collition- Geomagnetic Equilibrium, Journal of Atmospheric Sciences, 23, 1966.

Mallat, S.: A wavelet tour of signal processing, Academic press, 1999.

Matamba, T. M., Habarulema, J. B., and McKinnell, L.-A.: Statistical analysis of the ionospheric response during geomagnetic storm conditions over South Africa using ionosonde and GPS data, Space Weather, 13, 2015.

Mayr, H., Harris, I., Herrero, F., and Pesnell, W.: Transfer function model (TFM) and gravity Waves, Journal of Geomagnetism and Electricity, 43, 1991.

McNamara, L. F.: The Ionosphere: Communications, Surveillance, and Direction Finding, Krieger Publishing Company, 1991.

Midgley, J. E. and Liemohn, H. B.: Gravity Waves in a Realistic Atmosphere, Journal of Geophysical Research, 1966.

Misra, P. and Enge, P.: Global Positioning System: Signals, Measurements, and Performance, Ganga-Jamuna Press, 2006.

Moldwin, M.: An Introduction to Space Weather, Cambridge University, 2008.

Morton, F. and Essex, E.: Gravity wave observations at a southern hemisphere mid-latitude station using the total electron content technique, Journal of Atmospheric and Terrestrial Physics, 40, 1978.

Munro, G.: Travelling disturbances in the ionosphere, in: Proceedings of the Royal Society of London A: Mathematical, Physical and Engineering Sciences, vol. 202, 1950.

Munro, G.: Travelling ionospheric disturbances in the F-region, Australian Journal of Physics, 11, 1958.

Nappo, C.: An Introduction to Atmospheric Gravity Waves, Academic Press, 2002.

Ngwira, C. M., McKinnell, L.-A., Cilliers, P. J., and Yizengaw, E.: An investigation of ionospheric disturbances over South Africa during the magnetic storm on 15 May 2005, Advances in Space Research, 49, 2012.

Nishioka, M., Saito, A., and Tsugawa, T.: Super-medium-scale traveling ionospheric disturbance observed at midlatitude during the geomagnetic storm on 10 November 2004, Journal of Geophysical Research: Space Physics, 114, 2009.

Ogawa, T., N, N., Y, O., K, S., Tsugawa, T., and Hosokawa, K.: Medium-scale traveling ionospheric disturbances observed with the SuperDARN Hokkaido radar, all-sky imager, and GPS network and their relation to concurrent sporadic E irregularities, Journal of Geophysical Research, 114, 2009.

Ondoh, T. and Marubashi, K.: Science of Space Environment, Kanda Nishiki-cho, 2000.

Park, J., Lhr, H., Lee, C., Kim, Y. H., Jee, G., and Kim, J.-H.: A climatology of medium-scale gravity wave activity in the midlatitude/low-latitude daytime upper thermosphere as observed by CHAMP, Journal of Geophysical Research: Space Physics, 119, 2014.

Pedatella, N. M., Forbes, J. M., Maute, A., Richmond, A. D., Fang, T. W., Larson, K. M., and Millward, G.: Longitudinal variations in the F-region ionosphere and the topside ionosphere-plasmasphere: Observations and model simulations, Journal of Geophysical Research, 116, 2011.

Perna, L. and Pezzopane, M.: foF2 vs solar indices for the Rome station: Looking for the best general relation which is able to describe the anomalous minimum between cycles 23 and 24, Journal of Atmospheric and Terrestrial Physics, 148, 2016.

Press, W. H.: Numerical recipes 3rd edition: The art of scientific computing, Cambridge university press, 2007.

Prölss: Physics of the Earth's Space Environment: An Introduction, Springer-Verlag, 2004.

Raffel, M., Willert, C. E., Wereley, S. T., and Kompenhans, J.: Particle image velocimetry: a practical guide, Springer, 2013.

Ratcliffe, J. A.: Physics of the Upper Atmosphere, Academic Press, 1960.

Ratcliffe, J. A.: An Introduction to the Ionosphere and Magnetosphere, Cambridge University Press, 1972.

Rawer, K.: Wave propagation in the ionosphere, Kluwer Academic Publishers, 1993.

Rishbeth, H. and Garriott, O. K.: Introduction to Ionospheric Physics, Academic Press, 1969.

Rishbeth, H., Müller-Wodarg, I., Zou, L., Fuller-Rowell, T., Millward, G., Moffett, R., Idenden, D., and Aylward, A.: Annual and semiannual variations in the ionospheric F2-layer: II. Physical discussion, in: Annales Geophysicae, vol. 18, 2000.

Row, R. V.: Acoustic-gravity waves in the upper atmosphere due to a nuclear detonation and an earthquake, Journal of Geophysical Research, 72, 1967.

Samuel, H. F.: A theory of medium-scale traveling ionospheric disturbances, Journal of Geophysical Research, 79, 1974.

Seemala, G. K.: GPS-TEC analysis application, Institute for Scientific Research, Boston College, Boston, USA, 2004.

Sindelarova, T., Mosna, Z., Buresova, D., Chum, J., McKinnell, L.-A., and Athieno, R.: Observations of wave activity in the ionosphere over South Africa in geomagnetically quiet and disturbed periods, Advances in Space Research, 50, 2012.

Somsikov, V. M. and Ganguly, B.: On the formation of atmospheric inhomogeneities in the solar terminator region, Journal of Atmospheric and Terrestrial Physics, 57, 1991.

Somsikov, V. M. and Troitskiy, V.: Generation of disturbances in the atmosphere during the passage of the solar terminator, Geomagnetism and Aeronomy, 15, 1975.

Song, Q., Ding, F., Wan, W., Ning, B., Liu, L., Zhao, B., Li, Q., and Zhang, R.: Statistical study of large-scale traveling ionospheric disturbances generated by the solar terminator over China, Journal of Geophysical Research: Space Physics, 118, 2013.

Stamhuis, E. and Videler, J.: Quantitative flow analysis around aquatic animals using laser sheet particle image velocimetry, Journal of Experimental Biology, 198, 1995.

Stearns, S. D. and Hush, D. R.: Digital signal processing with examples in MATLAB®, CRC press, 2002.

Sutherland, B. R.: Internal Gravity Waves, 2010.

Taylor, J.: An introduction to error analysis: the study of uncertaities in physical measurements, University Science Books, 1997.

Thomas, J. A. and Smith, E. K.: A survey of the present knowledge of sporadic-E ionization, Journal of Atmospheric and Terrestrial Physics, 13, 1959.

Thome, D. G.: Incoherent scatter observations of traveling ionospheric disturbances, Journal of Geophysical Research, 65, 1960.

Thome, G.: Long-Period Waves Generated in the Polar Ionosphere during the Onset of Magnetic Storms, Journal of Geophysical Research: Space Science, 73, 1968.

Tolstoy, I.: Long-Period Gravity Waves in the Atmosphere, Journal of Geophysical Research, 72, 1967.

Torrence, C. and Compo, G. P.: A practical guide to wavelet analysis, Bulletin of the American Meteorological society, 79, 1998.

Tsurutani, B. T., Gonzalez, W. D., Kamide, Y., and Arballo, J. K.: Magnetic Storms, American Geophysical Union, 1997.

Tyalimpi, V. M.: Properties of traveling ionospheric disturbances (TIDs) over the Western Cape, South Africa, Master's thesis, Rhodes University, 2014.

Vadas, S. and Lui, H.: Generation of Large-Scale Gravity Waves and Neutral Winds in the Thermosphere from the Dissipation of Convectively Generated Gravity Waves, Journal of Geophysical Research, 114, 2009.

Van Der Mescht, D.: Mountain wave turbulence in the lee of the Hex River Mountains, Master's thesis, Stellenbosch University, 2012.

Verniani, F.: Developments in Atmospheric Science: Structure and Dynamics of the Upper Atmosphere, Elsever Scientific Publishing Company, 1974.

Westerweel, J.: Digital particle image velocimetry, Delft University, 1993.

Yeh, K. C.: Traveling ionospheric disturbance as diagnostic tool for thermospheric dynamics, Journal of Geophysical Research, 77, 1972.

Zhou, Y., Yang, J., Zhu, F., Su, F., Hu, L., and Zhai, W.: Ionospheric disturbances associated with the 2015 M7. 8 Nepal earthquake, Geodesy and Geodynamics, 8, 2017.

Zolesi, B. and Cander, R. L.: Ionospheric Prediction and Forecasting, Springer-Geophysics, 2014.

Zou, L., Rishbeth, H., Müller-Wodarg, I., Aylward, A., Millward, G., Fuller-Rowell, T., Idenden, D., and Moffett, R.: Annual and semiannual variations in the ionospheric F2-layer. I. Modelling, in: Annales Geophysicae, vol. 18, 2000.